Seminar series nr 174

Methane Emission Peaks from Permafrost Environments: Using Ultra–Wideband Spectroscopy, Sub-Surface Pressure Sensing and Finite Element Solving as Means of their Exploration

Norbert Pirk

2009
Department of Physics
Lund University
Sölvegatan 14
S-223 62 Lund
Sweden

Methane Emission Peaks from Permafrost Environments: Using Ultra–Wideband Spectroscopy, Sub-Surface Pressure Sensing and Finite Element Solving as Means of their Exploration

---

Norbert Pirk

Master degree thesis in Physics
Lund University
June 14, 2009

Supervisor: Torben Christensen
Department of Physical Geography and Ecosystem Analysis
Lund University

Abstract

Methane is an effective greenhouse gas of vital importance to global climate. Methane emissions from permafrost dominated peatlands contribute significantly to the dynamics of the high-latitude atmospheric methane concentration.

During the freezing period of autumn 2007 a large methane emission peak was recorded at a peatland in northeast Greenland. The integral of this abrupt peak was equivalent to the emissions of the entire summer season. The present work seeks to explain this unexpected methane burst.

A soil-vegetation-atmosphere transfer (SVAT) model based upon the finite element method is applied to simulate the methane emission driven by air temperature data from Greenland 2007. Laboratory experiments are developed in which the methane emissions from peat samples are monitored as they freeze. In order to relate the potential methane burst to the pressure build-up at freezing, sub-surface pressure sensors are employed. On another sample ultra-wideband microwave measurements are performed to capture gas dynamics inside the sample in a non-invasive manner.

It is found that a methane emission peak at the onset of freezing is not comprised in the SVAT model. Despite a significant pressure build-up, the methane discharge at the onset of freezing does not appear in the experiment either. Instead, a set of sudden methane bursts from the non-invasively treated sample are detected at the onset of thawing. Their occurrence is well captured in the signal response of the stimulated microwaves as well as in the attained dielectric permittivity. The volumetric content of gas, water and solid material is determined by the use of a dielectric mixing model. The results demonstrate the feasibility of ultra-wideband spectroscopy for gas movement processes in peat soils.

Sammanfattning

Metan är en effektiv växthusgas som har stor betydelse för det globala klimatet. Metan emissioner från våtmarker med underliggande permafrost anses bidra väsentligt till dynamiken som styr koncentrationen av metan i atmosfären på de nordliga breddgraderna.

Under nedfrysningen av marken hösten 2007 uppmättes ett stort utsläpp av metan vid en mätstation på nordöstra Grönland. Mängden metan motsvarade den totala mängden emission som uppmättes under hela sommarsäsongen. Denna rapport beskriver sökandet efter en förklaring till de oväntade mätningarna av metan.

En mark-vegetation-atmosfärs transport (SVAT) modell baserad på finita-element metoden tillämpas för att simulera metanemissioner med hjälp av lufttemperaturdata från Grönland under 2007. Laboratoriemetoder utvecklas i vilka metanutsläpp från torvprov kontrolleras vid nedfrysning. För att kunna relatera det potentiella utsläppet av metan till tryckansamling vid nedfrysning används trycksensorer. På ett annat torvprov utförs mätningar med ultra wideband mikrovågor för att mäta gas dynamiken inuti provet utan att tillföra yttre störningar.

Resultaten visar att SVAT modellen inte lyckas producera en emissionstopp då marken börjar att frysa. Trots en markant ansamling av tryck under nedfrysningen, uppkommer inte ett metanutsläpp i experimentet heller. Från torvprovet som behandlats utan yttre störningar, upptäcks istället en rad plötsliga metanutsläpp då provet börjar tina. Dessa händelser registrerades väl i signalresponsen av de stimulerade mikrovågorna samt i den uppnådda dielektriska permittiviteten. Volymen av gas, vatten och fast material bestäms med en dielektrisk mixing modell. Resultaten visar att denna metod är användbar för mätning av rörelseprocesser av gas i torv.

Contents

Chapter 1

Introduction

"Missing methane found at Zackenberg: Specialists in greenhouse gases have for some time wondered what the cause for the unexpectedly high concentrations of methane observed in the Arctic atmosphere during the autumn is. New research from Zackenberg Research Station shows that at least some of this methane might be squeezed out of the tundra in permafrost areas, when the upper part of the soil freezes in late autumn and in early winter. In the autumn of 2007 the tundra at Zackenberg contributed with more methane to the atmosphere during October than during the entire summer. The results have global significance due to the large areal extent of tundra areas with permafrost in Siberia and Northern Canada."
Quotation taken from the Zackenberg Research Station's website, www.g-e-m.dk/

A massive methane emission peak from high arctic permafrost environments has been found and actually no-one knows why. This report describes a Master thesis about the development of techniques for an explanation of this process. This project has been conducted as a cooperation of the Department of Physical Geography and Ecosystem Analysis, the Department of Electrical and Information Technology, and the Department of Physics, Lund University.

1.1 Motivation

Methane is the chemical compound with the molecular formula CH_4 and is a natural constituent of Earth's atmosphere. Whilst in the atmosphere, methane effectively absorbs infra-red radiation which makes it a strong greenhouse gas, in fact 22 times more potent than carbon dioxide. At present, methane alone contributes to about 22% of the greenhouse effect [Lelieveld et al., 1998] which is why the atmospheric methane concentration is of utter importance for the global climate. Currently the average methane concentration in air is about $1720ppb$ [Walter and Heimann, 2000], but unstable as sources and sinks are not in equilibrium.

Terrestrial wetlands represent the largest natural source of atmospheric methane [Mikaloff Fletcher et al., 2004]. Wetlands from high northern latitudes contribute significantly to the methane sources.

Peat soils form in wetlands and cover roughly 3% of the global land mass [Matthews and Fung, 1987] and contain about as much carbon as there is in the atmosphere [Clymo et al., 1998]. Peat is an accumulation of partially carbonized plants and other organic material that builds up in poorly drained wetland habitats. As peat keeps on growing it can reach depths of up to $10m$ over $10000years$, however the average depth is probably around $2m$ [Gorham, 1991]. Peatlands are a little unusual in their function for climate scenarios as they sequester carbon dioxide from the atmosphere as peat, whilst on the other hand they emit carbon dioxide and methane [Moore and Knowles, 1990].

Biogenic gases like methane are generated by methanogenic archea, then partly released into the atmosphere and partly stored in dissolved or free-phase form [Whiting and Chanton, 2001].

Permafrost is perennially frozen ground. Between the permafrost and the atmosphere there is typically a soil layer which thaws and freezes every year. This is called the active layer, as most of the dynamic processes occur here. Conditions for permafrost are mainly found in high northern latitudes, where the mean annual air temperature is below zero degree Celsius.

Figure 1.1: Zackenberg's location (74°30'N / 21°00'W) on Greenland

A large tundra methane burst during the onset of freezing was discovered at Zackenberg, Greenland, in autumn 2007 (cf. map in figure 1.1). Normally the station closes two month prior to this but as a part of the 2007 International Polar Year the measurements went on till October. At the station the methane flux is monitored with the help of Plexiglas chambers which close automatically once every hour to measure the methane concentration increase over 5 minutes.

The measured emissions show a connection to the ground temperatures, as shown in figure 1.2. The surprising thing about this data is the high peak in methane emission at the beginning of October. The total amount of methane emitted during these three weeks of freezing is equivalent to the total emissions of the rest of the year.

The peak occurs during a time when a production of methane in these amounts is unlikely. The low soil temperature does not allow for strong microbiological activity, so that this sudden release probably stems from an earlier production. Because the methane burst coincides with the onset of ground freezing, a connection to a suspected redistribution of stored methane by the frost action was proposed [Mastepanov et al., 2008]. Presumably the shielding of the permafrost bottom is necessary to prevent gases from moving downwards. A pressure build-up is suspected which squeezes the methane reservoir out of the soil. Other theories have been proposed (not yet published though) which see the reason for the burst in the sudden development of extremely anaerobic soil conditions when the uppermost soil layer freezes and thereby cuts off the oxygen supply for deeper layers, which then in turn produce methane. Yet another explanation is a dissimilar temperature response of different bacteria in the peat. Maybe the present methanogenic bacteria tolerate sub-zero temperatures more than the methanotrophic bacteria do.

To identify the correct explanation is the ultimate aim pursued in this work. Once the mechanism of the methane burst is understood, it can be implemented in climate models and improve their accuracy.

Note that this effect is probably a naturally occurring process, i.e. first and foremost independent of anthropogenic influence.

1.2 Approach

The investigation is started by a review of theoretical soil physics. Maybe this squeezing out of gases can be captured in a simple way by fluid- and thermodynamics. There might even be documentations of similar processes. Perhaps an existing soil-vegetation-atmosphere transfer (SVAT) model would be able to simulate the methane burst and one could thereby pinpoint its cause.

The experimental approach of this work comprises

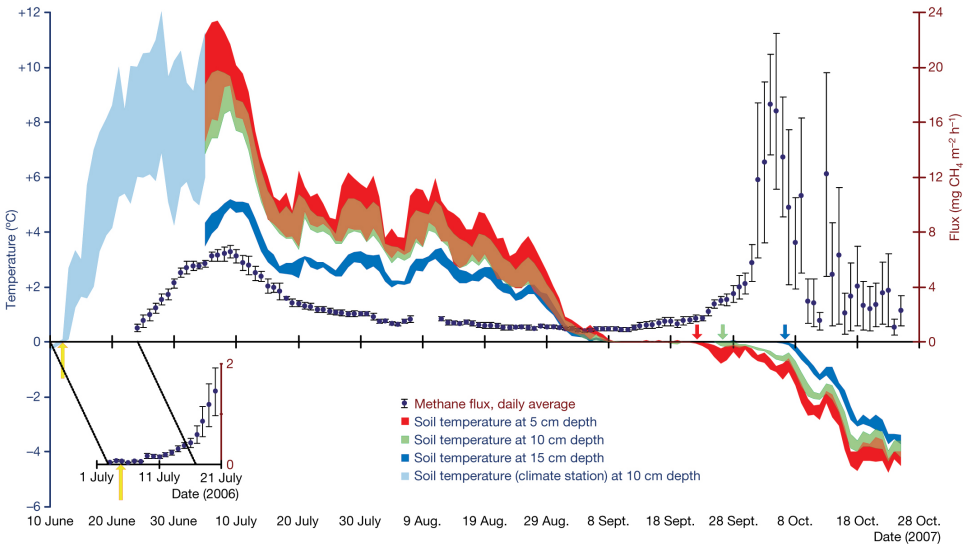

Figure 1.2: Measurements from Zackenberg, Greenland [Mastepanov et al., 2008]

measurements of peat soil samples which have been taken from a mire and treated under laboratory conditions. The idea is to monitor the gas dynamics of these samples while they freeze. This in itself constitutes a complicated task as the process is likely to be very susceptible to disturbances. The measurements from Greenland suggest that the soil freezes from its top down to its bottom. This so-called one-sided freezing has to be accomplished in the laboratory as well.

An ultra-wideband (UWB) spectroscopy setup is developed to track the distribution of biogenic gases within the sample.

Additionally, a gas pressure measurement is conducted in order to investigate a possible relation to the gas burst.

The hypothesis is that the observed methane burst is caused by a pressure build-up during the onset of freezing. No excessive methane production is the underlying reason, but it is a stored reservoir of methane which is squeezed out. That is to say that biological as well as chemical processes are of secondary importance for the explanation of the observed peak in methane emissions. This hypothesis relates to a set of questions which have to be answered in order to find a way of explaining the burst:

- Can the effect be captured in computer simulations?
- Is it possible to reproduce the methane burst with soil samples under laboratory conditions?
- How can such an experiment be set up?
- Could there be a correlation of the pressure and the surface flux?
- Is there a way to track the gas movement inside the peat?

The present work describes three independent methods used to explain the methane peak at the onset of freezing. Chapter 2 describes the theoretical basis of the used methods. It also contains information about the utilized instruments and equipment. Intermediate results of the pursue of an adequate setup are found in chapter 3. The final results of two freezing experiments are depicted at the end of chapter 3. Chapter 4 is dedicated to the discussion of the setup and the results attained by it.

Chapter 2

Methods

2.1 Theoretical Considerations

2.1.1 The Soil Freezing Problem

Soil freezing is an intricate physical problem of several interactive processes of heat and mass transfer. Its physical description is formulated by the fluid- and thermodynamics of an unsaturated porous medium. This medium is described as a soil matrix (skeleton), whose pores are filled with water, ice and gas.

Technically all of these components of the soil can move. Gas and water migrate through the soil matrix which can heave and subside. One can however differ between the more compressible components, like gas, and the more incompressible components like water. This classification is followed below.

The soil under consideration — in nature as well as in the laboratory — is embedded within its environment. Fluxes at the system's boundaries can violate the mass and energy conservation in the peat soil. The boundaries of the problem are the permafrost ground at the bottom and the atmosphere at the top. The permafrost is believed to constitute a barrier for the matter flow. The atmosphere is open to these flows. In the following, flow equations are discussed for the solution of which these boundary conditions become of crucial importance.

Temperature T and its change is the main driving variable in this process. The heat flow is caused by heat convection and conduction which act to even out temperature differences in the soil. Fourier's law describes the conductive heat flux q_{heat} as being proportional to the temperature gradient, i.e.

$$q_{heat} = -k_{heat} \nabla T. \tag{2.1}$$

The heat conductivity k_{heat} depends on the constitution of the soil, because the different materials have different individual thermal conductivities. Therefore, the heat flow depends on the soil composition which is why the mass and heat flow are coupled and can hence not be treated separately.

Besides the conductive heat flux, heat can be transported by the mass flow as convection. This is bound to mass transfer which is discussed below.

During the phase transition there will also be a latent heat flux which does not change the temperature. This creates a pressure instead which additionally effects the mass flow within the soil. The role of pressure is elaborated on in section 2.2.3.

Gas production and transport in the peat can occur by means of several mechanisms: Biological activity opens channels for mass transfer as it produces certain gases. Changes in local pressure or temperature can cause present free gas to expand or contract. Surface winds can pump in or suck out gases. The pressure deficit created by the extraction of soil moisture by plants draws air into the peat. Moreover, a potential water flow can carry dissolved gas through the peat as will be discussed later.

The continuity equation for a change in gas concentration can be written as

$$\frac{\partial c_g}{\partial t} = P + T \tag{2.2}$$

where c_g is the concentration of the respective gas, T includes all contributions from transport mechanism and P comprises all productions channels.

Under aerobic conditions, microorganisms within the soil consume oxygen and produce carbon dioxide, a process known as respiration. Under anaerobic conditions microbes produce methane. In the physical sense this means that there are sources and sinks of gases in the soil. The composition of soil air is characteristically different from that of atmospheric

air, as gases like methane and carbon dioxide appear in a lot higher amounts inside soils.

The path for most of the transport mechanisms T is the network of pores, which provides the connection between different peat layers. The two main processes, which operate in this pore network to effect the free gas transport, are mass convection and diffusion.

Convection is driven by gradients in total pressure, which cause the entire mass of air to move from a region of higher pressure to one of lower pressure. The convective gas flow is formulated by Darcy's law

$$q_g = -\frac{\rho k}{\eta} \nabla p \tag{2.3}$$

where q_g is the convective gas flux, ρ is the density of soil air, k is the permeability of the air-filled pore space, η is the viscosity of soil air and ∇p the pressure gradient.

Diffusion on the other hand arises due to a gradient in partial pressure (i.e. concentration) of any constituent member of the gaseous or liquid phase. An unevenly distributed constituent migrates from a region of higher concentration to one of lower concentration, while the fluid as a whole may remain stationary and isobaric. Fick's law describes the relation of this diffusive gas flux J_g to the gradient in concentration ∇c:

$$J_g = -D \nabla c \tag{2.4}$$

where D is the diffusion coefficient. D may differ depending on the phase in which the diffusion occurs, i.e. in the air-filled pores or a water film.

It is clear that plant roots enable further gas transport through both convection and conduction. This means that these structures influence the value of the diffusion coefficient and soil permeability. It also means that these parameters can differ at different positions in the soil — the soil becomes inhomogeneous. As roots grow in a preferential manner, this transport mechanism can even differ for different directions, which means the soil is not isotroph any longer.

The degree to which convective flows contribute to the exchange of gases between the soil and the atmosphere is a subject of debate among soil physicists [Hillel, 1998]. The relative importance of convection increases with pore size and proximity to the surface, but mostly, diffusion rather than convection appears to be the dominating process of gas transport.

The suspected reason for the methane emission peak from tundra wetlands however is a convective gas flux, caused by an excess in total pressure under the frozen peat layers. That is why the focus is put on the measurement of total pressure (cf. section (2.2.3) and the partial methane pressure is not investigated within this study.

The relation between pressure p, volume V, temperature T and the number of gas particles N of the gas is ideally given as

$$pV = N k_b T, \tag{2.5}$$

where k_b denotes Boltzmann's constant.

A simplified model of the an expanding membrane illustrates the suspected mechanism of the gas outburst. Imagine a gas reservoir with $N(t)$ particles and pressure $p(t)$ which is sealed to all sides but one. On this last side there is a membrane with a finite permeability K and thickness $d(t)$, symbolizing the layer of ice. On the other side of the membrane there is an atmosphere with a constant pressure p_{atmo}. The gas flux q through this membrane is described by Darcy's law (2.3) which can here be written as

$$\begin{aligned} q = \frac{\partial N}{\partial t} &= \frac{K}{\eta} \cdot \frac{p_{atmo} - p(t)}{d(t)} \\ &= \frac{K}{\eta} \cdot \frac{p_{atmo} - N(t) k_b T / V(t)}{d(t)} \end{aligned} \tag{2.6}$$

where η denotes the viscosity of the gas and the ideal gas law of equation (2.5) was used.

When now the freezing sets in, the membrane will expand and thereby initiate two counteracting processes: On the one hand it will compress the gas reservoir causing its pressure to increase. On the other hand the thickness of the membrane will increase as it grows. The pressure built up will drive the particle flux, whereas the increasing thickness will clog it. The pressure can be released by a particle flux through the membrane into the atmosphere.

A simple evaluation illustrates the process: The expanding membrane is modeled with the help of the unit step function $U(t)$, an example of which is displayed in the upper part of figure 2.1. Hence, the reservoir volume decreases as $U(t)$, whilst the membrane's thickness grows as $1 - U(t)$. For the sake of simplicity in the calculation the physical units are set aside and a relative time scale is used. K, T, k_b and η are all set to be equal *one*. An initial particle reservoir

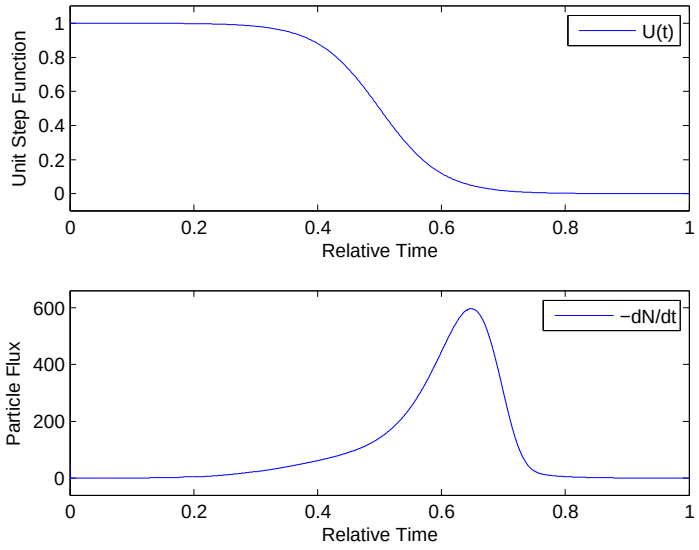

Figure 2.1: Simple model of a freezing membrane. Upper part: $U(t) = 1 - \frac{1}{exp(-20(t-0.5))+1}$. Lower part: Particle flux $\frac{\partial N}{\partial t}$

of $N_0 = 100$ is assumed and the atmospheric pressure is chosen to equal the initial reservoir pressure. The model is therefore reduced to

$$\frac{\partial N}{\partial t} = \frac{100 - \frac{N(t)}{U(t)}}{1 - U(t)}. \tag{2.7}$$

which is a first order differential equation for $N(t)$ which can be solved with one initial constraint. The lower part of figure 2.1 shows the resulting particle flux: An unsymmetrical peak which is centered around the optimal pressure-to-permeability ratio.

The transport of water is mathematically very similar to the transport of gases. The theory is analogous and therefore only touched here. Gradients in pressure, which is now called pressure head H, give rise to the water flow q_w, as described by Darcy's law $q_w = -K_h \nabla H$. Here K_h denotes the hydraulic conductivity, which can become a function of the water content Θ_w if unsaturated soils are regarded. Combining Darcy's law with the continuity equation for water flow

$$\frac{\partial \Theta_w}{\partial t} = \nabla \cdot q_w, \tag{2.8}$$

one gets the general flow equation

$$\frac{\partial \Theta_w}{\partial t} = \nabla \cdot K \nabla H - S, \tag{2.9}$$

where S represents the water uptake by roots [Schwarzel et al., 2006]. Equation (2.9) is often also referred to as Richards equation. If the soil is not fully saturated then the hydraulic conductivity becomes Θ_w-dependent. Θ_w itself is dependent on the pressure head H. Therefore the general water flow equation becomes a non-linear partial differential equation [Hansson et al., 2004].

The water flow contributes to the gas transport as well, as gases can be solved in the water.

The concentration of dissolved gases in a liquid generally increases with pressure and decreases with temperature. This is described by Henry's Law

$$c_m = s_c \frac{p_i}{p_t}, \tag{2.10}$$

where c_m is the concentration of the dissolved gas, s_c is its solubility, p_i is its partial pressure and p_t is the total pressure. The solubility s_c decreases with increasing temperature, so that cooler water can solve larger amounts of methane, for example.

During the phase transition of water to ice, the total pressure p_t can increase to such an extend that the methane molecules are forced to migrate into the water of the unfrozen parts of the soil. The dissolved methane flow which arises at the freezing boundary can exceed the methane diffusion flow in

water [Sigunov and Samylova, 2006]. As a result, the methane concentration near the ice surface increases and conditions for its passage from the solved phase into the free phase are produced. This can have a direct influence on the methane emissions during the onset of freezing.

The problem as described above is already very intricate. Nonetheless, there are a number of processes which have not even been mentioned.

Adsorption of water to soil particles, surface tension of the fluids, the capillary rise of the water table and hysteresis are a few of them.

Furthermore, water present in a soil is never chemically pure but has a certain salinity. Solutes in the water are known to have an effect on the amount of unfrozen water at subzero temperatures [Torrance and Schellekens, 2006]. Solutes as well as interactions of water with soil particles cause the so-called freezing point depression.

In nature, a soil is subject to all kinds of external perturbations, like clouds, cold waves, warm waves, rainstorms or snowstorms, and periods of drought. Externally exerted forces on the surface by the prevailing atmospheric pressure are to be mentioned. Earlier studies found a link between changes in atmospheric pressure and ebullition events [Kellner et al., 2004]. A snow pack blocks the heat and gas transport at the soil surface like an insulator. Needless to say that the infiltration of the peat by rain and runoff water becomes a relevant factor under natural conditions. Evaporation and percolation also change the water content directly.

The freezing and ice growth in frost-susceptible soils is another process contributing to the physics of the methane burst at the onset of freezing. The soil heaves due to a gradient in temperature within the ice, which triggers a process known as regelation: Ice at the warmer side of a soil particle melts and travels around the particle to its cold side where it refreezes again [Michalowski and Zhu, 2007]. As the soil particles are very much constrained in their movement, it is the ice which moves up and heaves the soil. Usually this occurs in the form of so-called ice lenses.

The coupled occurrence of these processes brings about a truly delicate problem of heat and mass transfer: The flows of mass and heat under non-isothermal conditions in a soil are interactive phenomena — one entails the other. Gradients in temperature induce gradients in matter density which cause a movement of the particles. The temperature field itself determines which phase the water is in. Reciprocally, gradients in moisture and pressure move the fluid components of the soil, which carries heat. Note how the mathematical structure of all the flow equations resemble each other.

This results in a system of coupled non-linear partial differential equations. There are no generally applicable methods to solve non-linear PDEs, and cases with analytical solutions are extremely rare [Richter, 1987]. For consistent boundary conditions, however, one has a fair chance of finding a numerical solution for the problem. This is where so-called finite element solvers enter the game (cf. section 2.1.2). There is a number of ways how mass and energy flow can be simulated based upon different assumptions. There is however no model known to the author which is primarily made to simulate gas dynamics in soils.

2.1.2 Modelling Approach

The mathematical model of the physical problem of soil freezing consists of a system of non-linear partial differential equations coupling thermal, mechanical and hydraulic aspects. The model is governed by the moving freezing front in which the physical parameters have discontinuities and the solution of the PDEs becomes non-smooth and sensitive to small perturbations [Hartikainen and Mikkola, 2001].

The finite element method (FEM) is a numerical technique for finding approximate solutions of partial differential equations. The basic idea is a discretization of the geometry of the given problem into pieces of finite dimension.

One defines a set of trial functions on this mesh of finite elements and assumes that a linear combination of these functions yields the real solution. The problem is now to find the coefficients of this linear combination for each of the finite elements. One inserts the linear combination together with all known boundary and initial conditions into the PDE which gives a coefficient matrix for each individual element. A joint matrix for the entire geometry is built by summing the individual ones. This matrix is numerically solved by a chosen algorithm, e.g. Gaussian elimination. These calculations can be performed in a steady or transient analysis. In the steady case one is looking for the state of the system at a given time, whereas the transient analysis yields all intermediate results as well.

The primary challenge is to create an equation which approximates the unknown real solution of the problem in a numerically stable way, meaning that errors in the input data do not accumulate during the intermediate calculation and cause the result to be meaningless. The stability has to be checked continuously by the solver [Potter, 1973].

The CoupModel is a one-dimensional soil-vegetation-atmosphere transport (SVAT) model developed to quantify basic hydrological and biological processes in the soil-plant-atmosphere system. It employs a transient finite element analysis to numerically solve a set of coupled differential equations. By dividing the depth profile of the soil into finite layers the model simulates different water, gas and heat processes.

Two coupled differential equations for water and heat flow represent the central part of the model. The basic assumptions behind these equations are the law of conservation of mass and energy, and that flows occur as a result of gradients in pressure (Darcy's law) or temperature (Fourier's law). The calculations of the water and heat flow are based on soil properties such as the water retention curve, functions for unsaturated and saturated hydraulic conductivity, the heat capacity including the latent heat at thawing/melting and functions for the thermal conductivity. The most important plant properties are included by the development of vertical root distributions, how the plants regulate water uptake from the soil and transpiration when stress occurs, and how the plant cover influences the aerodynamic conditions in the atmosphere.

All of the soil-plant-atmosphere system properties are represented as parameter values. Meteorological data are driving variables to the model. Most important of those are precipitation and air temperature, but also air humidity, wind speed and cloudiness can be used. Results of a simulation are such as temperature, content of ice, content of unfrozen water, vertical and horizontal flows of heat and water, water uptake by roots, frost depth, drainage flow and deep percolation to ground water.

In addition to the water and heat conditions also the plant dynamics and the related turnover of nitrogen and carbon may be simulated. The abiotic and biotic processes may be linked in different ways also to handle the feedback between the physical driving forces and the plant development. This makes a simulation of methane fluxes possible.

The CoupModel has several hundred different switches and parameters, which makes it very complex. This constitutes both an advantage and a disadvantage.

A FEM temperature field simulation is also used to investigate the efficiency of different cooling methods for our laboratory geometry. In order to estimate the time it takes the laboratory fridge to freeze the peat soil samples, a finite element solver is used to simulate the temperature distribution in two dimensions through time.

2.2 Experimental Method

2.2.1 Peat Sample Treatment

Special containers are needed for the samples. They must be made from plastic as metal would shield the inside from electromagnetic waves used to scan the sample (cf. section 2.2.5). Furthermore, they must not be shaped too conical, i.e. ideally their walls should be parallel. This is to make sure that the horizontal component of the developing ice pressure does not create a vertical force which pushes the peat soil up. Their height has to be of the order of a realistic active layer depth in a permafrost environment.

The containers of choice are $27cm \cdot 22cm \cdot 36cm$ in dimension. Their height of $22cm$ corresponds to a possible active layer depth found in the tundra.

Fäjemyr is a temperate, ombrotrophic bog in Scania, Sweden, which is used as a sampling site for the peat. Its long-term mean annual temperature (1961—1990) is 6.2^oC and its average precipitation is $700mm$. As the water table is generally below the surface, its topographical pattern becomes dominated by hummocks, lawns and carpets. Hollows and open pools are scarce. The rather dry conditions of Fäjemyr allow for an existence of dwarf shrubs, mainly Calluna vulgaris and Erica tetralix. The moss layer is dominated by Sphagnum magellanicum and Sphagnum rubellum. Sedges, mainly Eriophorum vaginatum, are prevalent as well. Fäjemyr is pictured in figure 2.2.

Four peat samples were taken March 30, 2009. Three of them were stored in a climate chamber at a constant temperature of 20^oC and a relative humidity of approximately 60%. Destilled water was added subsequently to account for evaporation. Thereby the water table was kept at a constant level of about $11cm$, corresponding to half of the container height. These warm and wet, anaerobic conditions were retained for the peat to produce a methane storage. At least one month of this incubation was estimated to accumulate a measureable amount of methane bubbles.

One of the samples was kept at only 5^oC room temperature. This temperature does not favor methane production, so that this sample would have significantly fewer methane than the other three. If this sample however gave the same emission peak during freezing, the peak could not be explained by means of a squeezed out methane storage.

For the freezing it is of vital importance to get the samples to freeze from the top to the bottom, as natural active layers would do in the autumn. Different methods were tried in order to accomplish this.

For the methane flux measurement (cf. section 2.2.4) air is needed to circulate to and from a chamber which is sealing the sample from above. The inflow was let through a freezer before entering the chamber in order to decrease the temperature and freeze the peat. This setup was not sufficient to freeze a small volume of water saturated soil, not to mention a real peat sample.

Therefore a thermal cycle was tried. Cooling agent was circulating in tubes between the interior of the freezer and the chamber on top of the sample. The thick layer of ice around the tube in the chamber suggested a working heat exchange inside the tubes. Nevertheless, the air and soil in the chamber did not cool down to sub-zero temperatures. Even a construction of thermal insulation around the sample could not stop the heat flow through the walls sufficiently enough.

Finally, the freezer was mounted up-side-down onto two hydraulic ramps. The container with peat was basically outside the freezer packed in thermal isolation, the chamber on its top however was in the interior of the freezer. This last technique was eventually used for the experiments.

The samples were consecutively frozen starting May 9, 2009. The top-down freezing is controlled by measurements of the temperature field inside the sample.

2.2.2 Temperature

Temperature is the main driving variable for the investigated process. Information about the temperature distribution is hence crucial for the understanding of its occurrence.

The temperature is logged by an *iButton Thermochron (DS1921G-F5)* manufactured by *Dallas Semiconductor*. In the range from -30^oC to 70^oC the sensor provides an accuracy of $\pm 1^oC$. The integrated memory can store up to 2000 time-temperature pairs. One of the sensors is directly mounted on one of the pressure sensors to seal its reference cell (cf. section 2.2.3). Another seven of them can be vertically distributed in the sample and used to produce a temperature profile through time. The sampling rate is chosen to $\frac{1}{5min}$.

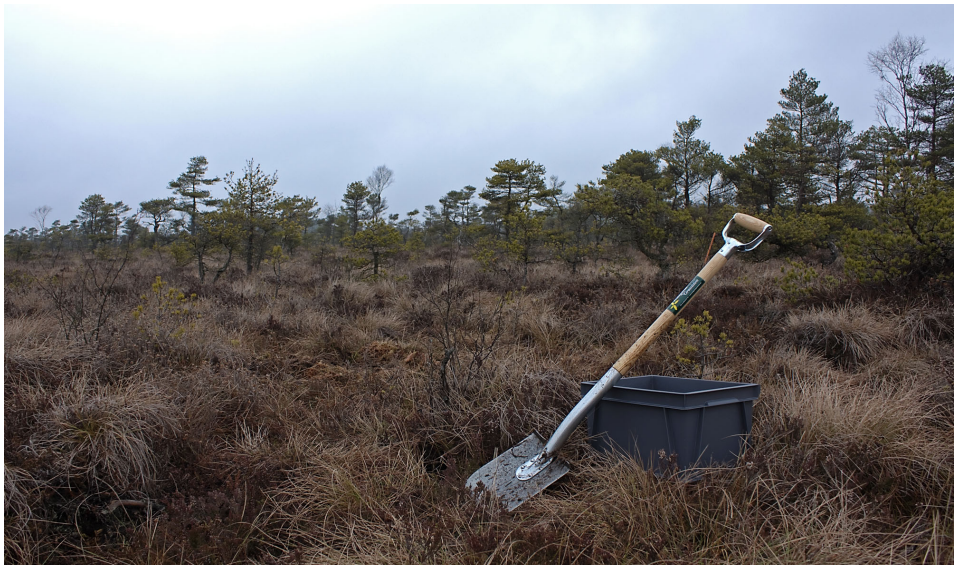

Figure 2.2: Sampling site Fäjemyr (56˚15'N / 13˚33'E), southern Sweden

This technique is very invasive as the sensors have to be implanted into the sample first. The idea was therefore to use these sensors and measure the temperature profile on one of the samples and extrapolate it to the others. Therefore, it was thought to utilize an infra-red thermometer to measure the temperature of the container walls. This value should somehow be related to the inside temperature. Assuming a linear relation between outside and inside temperature, one could calibrate the infra-red thermometer to yield a measure for the inside temperature, at a depth z and time t. The calibration would only be valid for this specific container and at a constant ambient room temperature. One would nevertheless be given the possibility to approximate $T(z,t)$ for the other samples non-invasively.

The developed setup for the freezing requires the actual sample to be embedded into thick thermal isolation. Hence it becomes rather complicated to reach the container wall frequently enough without disturbing the whole process. On account of this difficulty and possible interferences with the microwave scanning, it was chosen not to use the infra-red thermometer, but instead try to avail oneself of the gas flux measurement to estimate the temperature inside the samples without the *Thermochron* sensors. This is to say that the gas flux curve is mapped onto a curve of a sample with a known temperature distribution. Of course this requires that the implantion of the sensors does not change the gas flux dramatically. Assuming this, one can extrapolate the temperature profile of a measured sample to the others.

If for some reason this does not work, one can only estimate the temperature field for the undisturbed runs of the freezing experiment.

2.2.3 Total Pressure

As the hypothesis states a correlation of the methane burst to the total pressure, this is what is focused on here.

During the phase transition of water to ice, the density of the material decreases from about $1000\frac{kg}{m^3}$ to roughly $920\frac{kg}{m^3}$. This corresponds to a volumetric expansion of about 9%, which causes a pressure against adjacent material. To prevent water from expanding, the adjacent material must apply a tremendous pressure. This pressure, which keeps water from freezing, increases with lower temperatures. The phase interface between water and ice at constant volume is given by the Clapeyron equation

$$\frac{dp}{dT} = \frac{L}{T\Delta V} \tag{2.11}$$

where L is the latent heat, T is temperature and ΔV is the change in volume of the phase transition. For the water-ice transition with $T = 273K$, $L = 3.35 \cdot$

$10^5 \frac{J}{kg}$ and $\Delta V = -9.05 \cdot 10^{-5} \frac{m^3}{kg}$ one finds

$$\frac{dp}{dT} = -13.1 \cdot 10^6 \frac{Pa}{K}. \tag{2.12}$$

If the adjacent material was perfectly rigid, the ice would build up a pressure of $13.1 \cdot 10^6 Pa$ with each degree decrease in temperature. Usually, the adjacent material cannot withstand such a high pressure and deforms. Therefore this value constitutes the maximum pressure, which is hardly ever reached.

This is to say that the rigidity of the ambient material causes the pressure build-up. As ice and water are very much incompressible, the pressure between them can become extremely high. Air on the other hand is relatively easily compressible, so that the pressure in a gas bubble is only a fraction of the possible ice pressure from equation (2.12) as long as the increase in ice volume is smaller than the bubble volume. If however the expansion volume of the ice becomes of the order of the gas volume, a captured bubble will experience a pressure close to the full ice pressure. The volumetric gas content and pressure of its bubbles are thus intrinsically tied to one another, but even the finite compressibility of the peat structure can be of influence.

It is therefore hard to theoretically estimate the effective pressure which is to be expected in the measurement. It can furthermore not be excluded that the velocity of the freezing front plays an important role for the pressure build-up as well. For instance, stress within the ice could be released over time causing the pressure to decrease.

King and Fletcher [King and Fletcher, 1973] measured pressures of up to $90bar$ in $1cm$ wide water drops which were cooled to -5^oC. Having said that, Kellner et al [Kellner et al., 2004] reported a correlation between methane ebullition events from a fen peat and changes in atmospheric pressure, i.e. a fraction of one bar. Inside the peat they found overpressure zones of approximately $60mbar$, which were released suddenly as a result of a gas burst. This is to say that the decisive pressure in our experiment could range over orders of magnitude.

In a fluid, pressure is conducted equally to all directions, i.e. isotropically. The peat soil though contains a carbon skeleton and plant roots. When it freezes it also builds a network of ice crystals. These structures conduct a pressure a bit like arches of a Gothic cathedral. A deeper soil layer could therefore be shielded as a part of the pressure from above it is led to the container walls. As long as the water content is very high this effect is negligible. Yet at sub-zero temperatures this so-called dilatancy should be given some consideration.

For the measurement, different methods and sensors are tried out. If the method was not sensitive enough, its signal would be insignificant and therefore of little use. If, on the other hand, the pressures exceeded the sensor's measurement range, the instrument could break, which would also only give little information about the process dynamics.

There are different ways of getting a measure for the pressure the gas is exposed to. Inserting a tube into a container wall gives a measure for the water head at the height it is connected to the container. The water column in the tube rises with increasing pressure in the sample. Employing tubes at different heights and reading off their water table can therefore measure the pressure, as long as the water in the tube is mobile. As the experiment is conducted at sub zero temperatures this technique is not the first choice.

Another way of measuring is to insert a test specimen as a sensor. This entails an inflicted disturbance which can become crucial for the gas dynamics inside the sample. Implanting a sensor into the soil can hardly be done without pressing out stored gases, which are the believed reason for the methane burst. Once the sensor is inside the sample, it can be thought of as an artificial test gas bubble. The mere presence of it, nevertheless, influences the pressure especially towards the completion of freezing when the unfrozen liquid volume becomes of the order of the instrument's dead-space volume. Furthermore, Kellner et al [Kellner et al., 2004] reported that a pressure build-up can be released by gases escaping via a channel created by the sensor cable or tube. This can be circumvented using wireless sensors, which in turn become bigger as they carry batteries and data memory.

The sensor can be a rubber ball filled with a fluid. If the ball is connected to the ambient atmosphere via a U-shaped tube with water in it, the pressure difference can be read off. This method was tried in field experiments with a moderate success. They could show the rising pressure qualitatively, but not quantitatively.

To capture the pressure electronically, one can use a variety of physical effects. One way is to utilize the ability of some materials to change their resistivity in response to applied mechanical stress. This effect is known as piezo-resistivity and is particu-

larly pronounced in semiconductors. The mechanical deformation of the material causes a change in its charge carrier density and therefore its resistivity. As semiconductors have a very limited amount of charge carriers, the piezo-resistive effect becomes relatively strong. Using thin- or thick-film technology one deposes a piezo-resistive layer on a carrier plate to create a so-called strain gauge. One therewith builds a membrane, which changes its resistivity proportional to the pressure difference between its two sides. Typically, one side of this membrane is connected to a sealed reference cell which contains a captured fluid. Such an instrument is then referred to as sealed resistance strain gauge-pressure sensor.

The working principle of these pressure sensors is based upon the mechanical deformation of an interface. Accordingly, the material which exerts the pressure on the interface has to be mobile, i.e. fluid. It is therefore not only the measuring range of the sensor, but also the mechanism of the pressure transfer to its membrane which determines the result. A frozen peat soil is really barely fluid, so that the pressure from the solid state has to be transferred to the membrane somehow before the actual detection. It is however possible that this transfer does not work one-to-one, because of the inner structure of the transfer process.

To finally check the sensor's functionality, one could try to vary the pressure at the surface once the sample is frozen in. If the sensor still responds from under the frozen peat it is well suited for the measurement. If one wants to capture the thawing process however, one cannot disturb the sample too much when it is frozen.

In default of an existing solution, industrial pressure sensors are utilized. Two different resistance strain gauge-pressure sensors are used, one based on thin-, the other on thick-film technology. In general, thin- and thick-film sensors have similar characteristics [Bergmann et al., 1992].

The *Hygrosens DS-KE-R* thick-film sensor is designed for an application in hydraulic or pneumatic machines. It consists of a membrane on a ceramic ring which deforms in response to a pressure difference. Its measuring range goes to $400kPa$ and its burst pressure is $1000kPa$. The sensor is made up as a full Wheatstone bridge which gives an un-amplified output voltage in the order of millivolts. In order to utilize this device, a reference cell (or artificial bubble) is built by sealing the ceramic ring with a rigid metal plate. This metal plate is actually the bottom part of an *iButton Thermochron (DS1921G-F5)* temperature logger, which was glued onto the ring. The sealing is performed at approximately standard conditions for temperature and pressure, i.e. 20^oC and $100kPa$. In doing so one closes in a cylindrical volume of $\pi \cdot (5mm)^2 \cdot 6mm$, allowably a huge volume for a real peat bubble. The calibration curves of the sensor are shown in figure 4.3 in the appendix.

The *Motorola MPX 4250 AP* was built for the automotive industry to measure the intake of motor suction systems. It uses thin-film technology to measure fluid pressures from $20kPa$ to $250kPa$. Its burst pressure is $1000kPa$ as well. This sensor operates on a $5V$ input signal which is provided by a 7805 voltage regulator. The sensor is wired as shown in figure 4.1 (appendix) to avoid a malfunction caused by noise which is received by the cables and possible self-oscillations of the integrated circuits. This circuit is set up according to the specifications given by the manufacturer. The *MPX 4250 AP* already has its own reference cell which is connected to the environment by a small tube. The sensor is inserted into the soil with the open tube pointing downwards, so that some air is left in the tube. Unlike the *DS-KE-R* however, this air has a way to escape if it manages to penetrate through the adjacent material. The sensor comes pre-calibrated.

Additionally, a *HOBO U20-001-01* wireless water level and temperature logger is employed. It is originally designed to measure depths of wells or others waterbodies and is equipped with an absolute pressure sensor encapsulated in ceramic. It is operating up to $207kPa$ with a burst pressure of $310kPa$. Its specification does however not give information about the technique used.

The electronics of the sensors are temperature-compensated and provide a remarkable linearity of their signals within the measurement range. One must nonetheless be aware of what the output values mean. The *DS-KE-R* gives the pressure on a hypothetical bubble whose gas is trapped and cannot move or escape anywhere. The measurement hence becomes temperature dependent again, because the trapped gas adepts the ambient temperature and therefore changes its counter pressure. The signal *MPX 4250 AP* is subject to the same effect, although here the hypothetical bubble is free to escape, if its pressure exceeds a threshold. The *HOBO U20-001-01* on the other hand does not have any transfer gas but measures directly in its surrounding. Table 2.1 lists the three as an overview.

Sensor	Technique	Measurement Range [kPa]	Accuracy [Percent FS]
Hygrosens DS-KE-R	Thick-film, sealed bubble	up to 400	±1.5
Motorola MPX 4250 AP	Thin-film, open bubble	20 to 250	±1.5
HOBO U20-001-01	Open	up to 200	±0.1

Table 2.1: Overview of the used pressure sensors

2.2.4 Methane Flux

The measurement of the methane flux from the sample's surface is attained by means of a time record of methane concentrations within a chamber on top of the sample. These chambers (dimension: $28cm \cdot 34cm \cdot 38cm$) are made from Plexiglas and put on top of the containers, where the joint is sealed with silicon. A little fan provides a reliable mixing of the air inside the chamber. This system is assumed to be airtight, apart from one inflow and one outflow tube which are needed for the gas analysis. The air streaming into the chamber has atmospheric concentrations of methane and carbon dioxide. The air streaming out of the chamber is pumped into an *Innova AirTech Instruments 1312 Photoacoustic Multi-gas Monitor* which measures the particle concentration of not only methane, but also carbon dioxide and water vapor. The concentration difference between in- and outflow is used to calculate the gas flux from the peat sample.

The gas analyzer works on the basis of photoacoustic infra-red spectroscopy: Gas is pumped into its analysis cell which is then sealed hermetically by closing in- and outlet valves. Light of an infra-red source passes through a mechanical chopper which pulsates it, and then through an optical filter which selects a bandwidth around an absorption line of the respective gas. Then the light traverses the analysis cell, causing the temperature of its gas to increase. As the light is pulsating the gas temperature increases and decreases with the pulse frequency. This causes an equivalent oscillation of the pressure in the sealed analysis cell which gives an acoustic signal. Two microphones mounted in the cell wall measure the amplitude of this signal which is directly proportional to the concentration of the monitored gas present in the cell. Before the sample gas is released again, the optical filter is switched to measure the other gas components as well. In doing so, the instrument completes one measurement cycle in a little less than one minute. This time resolution is considered well suited for the investigation of possible methane bursts.

Unfortunately, the output of this method depends on the temperature of the analysis cell. As the ambient room temperature varies a little over time, an error is inflicted on the measurement.

As an expression for the respective surface flux F at time point t_i one uses

$$F(t_i) = \frac{p \cdot M_{mol}}{T \cdot R \cdot A} \cdot \left(f \cdot \Delta N_i + V \cdot \frac{\Delta N_i - \Delta N_{i-1}}{t_i - t_{i-1}} \right) \tag{2.13}$$

where p and T are the chamber's pressure and temperature, M_{mol} is the molar weight of the respective gas, R is the gas constant, A is the surface area of the sample, f is the flowrate through the chamber, ΔN_i is the difference of the gas particle number from before and after the chamber at time t_i and V is the chamber's volume.

The term with the flowrate f relates the surface emissions from the sample to the gas outflow from the chamber. This alone disregards the inertia introduced by the finite chamber volume, which smears out variations in the flux. The $\frac{\Delta N_i - \Delta N_{i-1}}{t_i - t_{i-1}}$ term however accounts for this in a first approximation. This 'sharpens' the emission peaks which occur on short time scales. In a mathematical sense, this resembles a deconvolution of the signal.

2.2.5 Ultra-wideband Spectroscopy

The mechanisms of formation and spatial distribution of free-phase biogenic gases in soils are theoretically well described (cf. section 2.1). In practice however there is still a considerable uncertainty about it [Comas and Slater, 2007], in particular in the case of a freezing soil. In order to understand the methane burst at the onset of freezing, an interest in a measurement of gas content and peat structure arose.

If one was given knowledge about the soil's gas content, one could examine where the gas flux comes from and how it was initiated. If methane is really squeezed out of the peat, the gain of methane above the soil should coincide with a loss of gas in-

side of it. One could look for patterns in the gas dynamics and possibly find the reason for the methane emission peak. One cannot expect to measure the methane content directly, but a measure of the volumetric gas content in the peat can be used to infer to the methane content.

Methods for studying gas dynamics in peat soils are usually a compromise: They are either rather destructive when one implements sensors into the sample, or they cannot give any spatial discrimination because they are applied outside the sample as in the case of the surface elevation for instance.

Other techniques circumvent this compromise. X-ray computed tomography has been shown to yield extremely sharp pictures of peat soils [Kettridge and Binley, 2008]. Ultra sound sensing and nuclear magnetic resonance tomography are other possibilities of a non-invasive examination of the process. For different reasons these technologies are not at our disposal for this project.

The approach chosen here to investigate the peat is to utilize its dielectric properties and the way they relate to its composites. One of these properties is the relative complex dielectric permittivity, denoted as ε. This complex number describes how an electric field propagates through matter. In free space for example, electromagnetic waves propagate at the speed of light and without losing energy. When waves travel through a dielectric matter however, they are slowed down and attenuated. The velocity of the wave (or signal) is given by the real part of ε, and its attenuation relates to the imaginary part of ε. Through this parameter ε the material provides a lot of information about itself. Ultra-wideband spectroscopy (UWB) is one technique which can be used to measure ε.

The signals transmitted by the antennas of this method are very weak. UWB works virtually non-invasively and will here be used to measure the volumetric gas content of the peat sample as a function of time.

The mixing of the individual materials to the bulk dielectricity was first modeled by Lichtenecker [Lichtenecker, 1926]. Accordingly,

$$\varepsilon_{bulk}^{\alpha} = \sum_i \Theta_i \varepsilon_i^{\alpha} \tag{2.14}$$

where i stands for the single constituents of the bulk. Θ_i denotes the respective volumetric content and ε_i stands for the relative dielectric permittivity. The parameter α can range between -1 and 1, and describes the arrangement of the constituents to each other. For a homogeneous mixture its theoretical values is 0.5. Some calibrations in soil science found better fits for their measurements when α was slightly different from 0.5, but the use of values different from the theoretical value 0.5 has not yet been justified [Zakri et al., 1998]. Equation (2.14) is referred to as Lichtenecker's mixture formula and was originally derived in an empirical way. It could later be put on a theoretical basis by effective medium theory. Note that ε is a complex number, i.e.

$$\varepsilon = \varepsilon' - i\varepsilon'' \tag{2.15}$$

where ε' is the real part whilst ε'' denotes the imaginary part. Thus equation (2.14) decomposes into a real and an imaginary part. Although widely accepted, Lichtenecker's equation is not without controversy. For example some critics point out that the exponent α is not only dependent upon the geometrical structure of the mixture, but also depends on the permittivity contrast between the different phases [Brovelli and Cassiani, 2008]. The equation will here be assumed to be well satisfied at all times.

The dielectric properties of the participating materials is of substantial importance for the mixing model. The final result for the volumetric fractions Θ_i will depend on the correct measurement of ε_{bulk} and the correct values for the individual permittivities ε_i. Single materials are well described by the Debye theory for dielectric relaxation, which has been attested in numerous of experiments. It predicts the response of a population of ideal, non magnetic, non interacting dipoles to an alternating external electric field. Each material is assigned three parameters which describe how its electric dipoles behave when excited by different frequencies ω. According to Debye

$$\varepsilon(\omega) = \varepsilon_\infty + \frac{\varepsilon_{dc} - \varepsilon_\infty}{1 + i\omega\tau} - i\frac{\sigma}{\omega} \tag{2.16}$$

where ε_{dc} represents the static dielectric permittivity, ε_∞ is the permittivity at infinitely high frequencies and τ is the relaxation time of the material. The last term containing the electrical conductivity σ diminishes at higher frequencies. At the range around 1GHz its contribution becomes neglectable. These Debye parameters are in general functions of the tem-

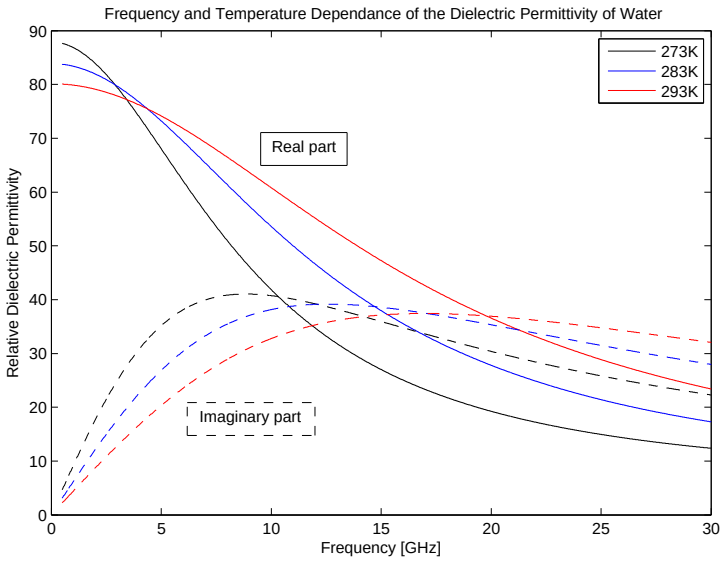

Figure 2.3: Dielectric properties of free water in Debye theory

perature. Figure 2.3 illustrates $\varepsilon_{water}(\omega)$ for different temperatures.

Fortunately, not all materials are as complicated as water. As a matter of fact, ice, soil and air are barely dielectric at the GHz range.

Air can be assumed to behave like free space.

For peat the values of ε' differ a little, from about 2 [Comas and Slater, 2007] to 4.7 [Lin, 2003], but constant over the used frequencies. The imaginary part ε'' is evanescent in the GHz range due to the low relaxation frequency of some kHz.

In [Jiang and Wu, 2004] different measurements and models for ice are discussed. At frequencies between $1GHz$ and $10GHz$, ε'' is constant with a value of 0.005. ε' is constant over frequencies as well, with a value of 3.15. As these values carry a little temperature dependence, ice is regarded to be at -3^oC.

The values for these parameters could be measured using UWB, and these measurements would be very interesting. Because the aim here is a different one, the literature values are used for later calculations. Table 2.2 shows the values assumed for the mixing model used here.

Note how similar ice and peat are dielectrically. Both have no attenuation in the lower GHz range, and a constant ε' of around 3. As the volumetric ice and peat content are of no special interest, one does not have to make an effort to separate these two components. For the mixing model they are therefore taken as one and the same material, referred to as the solid phase.

This reduces the number of free parameters of equation (2.14) to three: Θ_{gas}, Θ_{water} and Θ_{solid}. Another one of these parameters is fixed by the constaint that the volumetric fractions have to sum up to *one*, i.e.

$$\Theta_{gas} + \Theta_{water} + \Theta_{solid} = 1. \tag{2.17}$$

Together with the complex value equation (2.14) which yields another two constraints if ε_{bulk} is known, one can solve for the three volumetric fractions, for each point in time. Note however, that when equation (2.14) is decomposed to its real and imaginary part, the two resulting equations are not linear in Θ_i any more. The evaluation of this set of equations is hence done numerically in a grid search over the three volumetric contents, constrained to equation (2.17).

The soil dielectric properties can differ from the mere sum of all its constituents. Interactions at the interfaces between the constituents can cause a change in the dielectric properties of the interacting molecules.

The water-air interface around bubbles is polarized by the spontaneous orientation of water dipoles at the phase boundary, giving rise to the bubbles' surface tension. The surface water dipoles are oriented at the interface so that their stronger electric

	Gas	Water	Solid
ε'	1	Debye Model	3.150
ε''	0	Debye Model	0.005

Table 2.2: Assumed dielectricities for different pure materials

field (hydrogen atoms) is directed into the phase of higher dielectric permittivity (water), and the oxygen atom is directed towards the air [Hurd et al., 1962]. The number of these surface molecules in the soil is orders of magnitude smaller than the number of bulk molecules, so that such effects are assumed of evanescent importance.

A similar effect, known as adsorption, occurs at the water-soil-particle interface. Water molecules close to soil particles experience attractive forces and thus lose a part of their polarizability. This so-called bound water has a relaxation frequency $f_{rel} \approx 9GHz$ [Lin, 2003] which means its attenuation at frequencies from roughly $1GHz$ to $10GHz$ is higher than the free water attenuation. Static and high frequency value of water does not change when its bound to soil particles. Apart from potential gas bubbles, the soil investigated here is well water saturated. Again this means that the fraction of bound water molecules to free water molecules is extremely small.

The electrical conductivity for direct currents σ is zero for pure water, ice and soil particles. Just a little bit of salt within the soil, however, can make it conductive for direct currents. This finite soil conductivity is usually assumed to be the sum of the pore water conductivity and the surface water conductivity. Its contribution to the dielectric permittivity decreases with an increasing frequency (cf. equation (2.16)). At frequencies around $1GHz$ and higher, ε depends only weakly on salinity [Wensink, 1993]. The high frequencies used in this experiment justify the neglection of soil salinity.

Within the field of soil sciences, time-domain reflectometry (TDR) is often used to measure ε and thereby calculate the volumetric contents. Microwave pulses are sent through the medium of interest and their propagation is recorded. These so-called ground-penetrating radars (GPR) can be used to map an area in order to find subsurface structures like landmines, archaeological features or a resource deposit [Huisman et al., 2003].

If the pulse is transmitted and received by the same antenna, the reflected signal, S_{11}, is recorded. If a second antenna is used to record the pulse, the signal is referred to as S_{21}. If the investigated medium is placed between the two antennas the technique is sometimes called transmissometry, because one usually aims to detect the transmitted pulse (although reflections from ambient objects contribute to the signal).

TDR requires a device which can generate a strong and sharp pulse. As this is a rather delicate and expensive issue, one can avail oneself of Fourier's theorem which states that any periodic signal X can be transformed to another domain. Accordingly, a signal in the time domain can be transformed into an equivalent signal in the frequency domain. If X is defined at N discrete frequencies ω_j, its Fourier transformation x can be calculated for the N times t_k, and vice versa. This case of the Fourier transformation (and its inverse) is implemented as

$$\begin{aligned} x(t_k) &= \sum_{j=1}^{N} X(\omega_j) e^{2\pi i(\omega_j - 1)(t_k - 1)/N} \\ X(\omega_j) &= \tfrac{1}{N} \sum_{k=1}^{N} x(t_k) e^{-2\pi i(\omega_j - 1)(t_k - 1)/N}. \end{aligned} \tag{2.18}$$

If N is large enough, one usually neglects the discreetness of the signals and omits the indices k and j. As this transformation is reversible, both $x(t)$ and $X(\omega)$ carry that same information regardless of their domain. On the basis of this theorem, one can perform the entire analysis of the dielectric properties in the frequency domain. One measures the material's response for a set of frequencies within a bandwidth individually, i.e. one excites sinusoidal signals with different frequencies and thereby generates a virtual time domain. An ideally flat frequency signal becomes a *sinc* pulse in the time domain. In reality the energy radiated by an antenna varies over frequency, so that a flat signal can only be provided over a certain range of frequencies.

For many purposes of TDR only the time of arrival of the pulse is used. One uses that the real part of the dielectric permittivity ε' relates to the wave's velocity

inside the medium as

$$v = \frac{c_0}{\sqrt{\varepsilon'}}. \tag{2.19}$$

Often this velocity v is measured and the according ε' is used for the dielectric mixing model (cf. equation (2.14)). The material in itself however provides more information which lies in the strength of the received signal. This information becomes available in the frequency domain as one measures both phase and amplitude of the received waves.

Using a setup with two antennas provides another advantage: One can not only measured the transmitted part of the signal S_{21}, but also the reflected part S_{11}. Although the reflected signal scans the sample in a different manner, the two signals carry the same information about the material, in principle. Consequently, a measurement of both helps to increase the accuracy in reality.

The main problem is to identify the desired peaks in transmitted energy from other signals which found their way to the receiver. There is not only the noise background on the measured signal, but in principle also a contribution from any possible path between the transmitter and the receiver. The signal prefers to take the way of least resistance (dielectric permittivity) and it is an art in itself to get the waves to take the exact path one wants them to take. Creeping waves around the sample and unintentional reflections have to be minimized. This is why one prefers to have small samples which fit in shielded cables, instead of measuring in a free space experiment.

The means one has to solve this are amongst others the utilization of electromagnetic absorbers, the variation of the used frequency band and a geometrical change of the setup. How this problem is approached is addressed in section 3.3.

The theory of wave transmission is well described in the literature, [Hallikainen et al., 1985] or [Håkansson et al., 2007], and will here mainly be stated. Accordingly, the transmission coefficient of an infinite slab of length L is known to be

$$S_{21}(f) = |S_{21}(f)|\, e^{i\phi_{21}} = \frac{\left(1-R^2\right) e^{-\gamma L}}{1-R^2 e^{-2\gamma L}} \tag{2.20}$$

and the corresponding reflection coefficient is given by

$$S_{11}(f) = |S_{11}(f)|\, e^{i\phi_{11}} = \frac{\left(1-e^{-2\gamma L}\right) R}{1-R^2 e^{-2\gamma L}}. \tag{2.21}$$

Here γ, the propagation constant of the dielectric-filled slab, is defined in terms of the attenuation coefficient α and the phase factor β as

$$\gamma = \alpha + i\beta = \frac{2\pi}{\lambda_0}\sqrt{-\varepsilon} \tag{2.22}$$

where $\frac{2\pi}{\lambda_0} = k_0$ is the wavenumber in free space, λ_0 is the free space wavelength, and ε again denotes the relative complex dielectric permittivity of the sample as defined in equation (2.15).

From the above, ε' and ε'' can also be calculated by

$$\varepsilon' = \left(\frac{1}{k_0}\right)^2 \left[-\left(\alpha^2-\beta^2\right)\right] \tag{2.23}$$

$$\varepsilon'' = \left(\frac{1}{k_0}\right)^2 (2\alpha\beta). \tag{2.24}$$

The field reflection coefficient R is given in terms of Z_0, the intrinsic impedance of free space, and Z, the characteristic impedance of the dielectric-filled slab, as

$$R = \frac{Z - Z_0}{Z + Z_0}. \tag{2.25}$$

These impedances are given by

$$Z = \frac{i\omega\mu_0}{\gamma} = \frac{2\pi\eta_0}{\lambda_0} \cdot \frac{\beta\left(1 + i\alpha/\beta\right)}{\alpha^2+\beta^2} \tag{2.26}$$

$$Z_0 = \mu_0 c_0 = \sqrt{\frac{\mu_0}{\varepsilon_0}} \tag{2.27}$$

$$\mu_0 = 4\pi \cdot 10^{-7} \tag{2.28}$$

$$\varepsilon_0 = \frac{1}{\mu_0 c_0^2} \tag{2.29}$$

$$c_0 = 2.9979 \cdot 10^8 \tag{2.30}$$

where $\omega = 2\pi f$ is the angular velocity at frequency f, μ_0 is the permeability of free space and ε_0 is the electric constant.

The heart of the setup is the vector network analyzer (VNA) which generates the input signal and evaluates the output signal. What is actually recorded by the VNA is the ratio of the phase and the amplitude between the sent and received signal. It is connected to the two antennas, where the received side contains amplification. The way these are set up is shown in figure 2.4, and the way this setup was obtained is elaborated on in section 3.3.

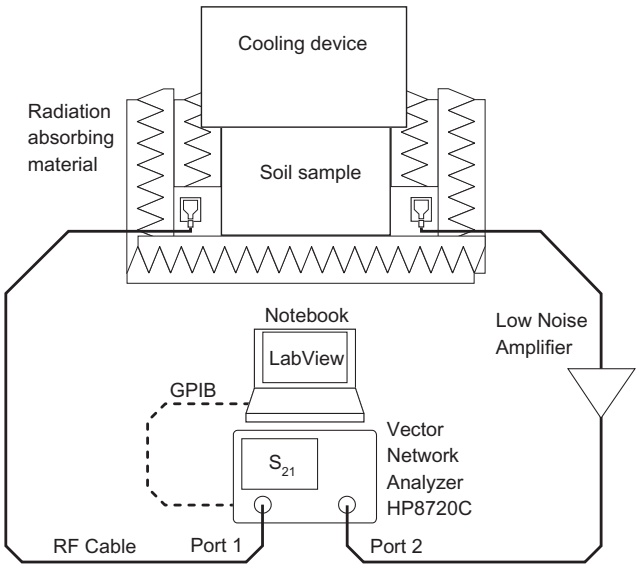

Figure 2.4: Measurement diagram

Processing and calibration of the measured signal is needed before any calculations of the dielectric constant can be performed correctly. When transmission measurements are done through a sample, the recorded S_{21} parameter includes not only the influence of the sample under test but also cables, amplifier and antenna distortions. To correct for this, the measured coefficients must be calibrated. A simple way to perform this calibration is to do it directly in the frequency domain by a division

$$S_{21,sample}(f) = \frac{S_{21,measured}(f)}{S_{21,calibration}(f)}. \tag{2.31}$$

It is important to note that calibrations performed directly by a division are valid only under certain conditions. One condition is that the system must be linear, which means that the introduction of a certain material in the box must not generate new channel components. This is often not the case as materials with $\varepsilon' > 1$ generate diffractive fields around the sample and create new reflection components from within the sample. To find the correction coefficients, $S_{21,calibration}(f)$, it was started by measuring the transmission through an empty box $S_{21,free-space}(f)$, which contains all the abovementioned non-linearities. Ideally, $S_{21,calibration}(f)$ should be the transmission coefficient for when there is no sample at all, such that the antennas would have to be almost touching each other. This is not possible since the two antennas would stop behaving as good radiators due to the coupling between each other (near field effects). Therefore the approach is to first measure the empty box (free space), and then "back-rotate" the phase of each one of the frequency points by an amount corresponding to the length of the box, L, assuming propagation at the speed of light. In this way, one eliminates the influence of the unwanted free space within the box. Accordingly,

$$S_{21,calibration}(f) = S_{21,free-space}(f) \cdot e^{i2\pi Lf/c_0}. \tag{2.32}$$

This approach also solves an additional problem. The assumption in equations (2.20) and (2.21) is that the wave impinging on the slab is plane or lossless, which is not the case since the waves radiated by the antennas are spherical, i.e. lossy. However, by only "back-rotating" the phases in (2.32), $S_{21,calibration}(f)$ also contains that loss in free space, which will then also be corrected.

The calculation of the bulk Dielectric Permittivity ε_b is performed by a grid search which minimizes the difference to the measured signal, i.e.

$$\varepsilon_b(f) = \varepsilon_b' - i\varepsilon_b'' = \arg\min_{\varepsilon_b} \left| S_{21,sample}(f) - \frac{\left(1-R^2\right) e^{-\gamma L}}{1 - R^2 e^{-2\gamma L}} \right|. \tag{2.33}$$

Unfortunately, this equation has infinite solutions. To step over this obstacle one can make use of the ap-

proximation that consecutive frequencies have similar ε_b and calculate it starting from a reasonable initial guess.

Chapter 3

Results

3.1 SVAT Simulations

The CoupModel was set up to solve the equations for water, gas and heat flow. To drive the model, measured temperatures from Zackenberg 2007 were used (not shown here). Because no data on precipitation was available it was switched off by the parameters, whilst at the same time water evaporation, soil drainage and deep percolation were switched off as well. This keeps the soil at a constant total moisture. By setting the mean annual air temperature to a value below zero degrees Celsius, the permafrost ground was established. The bottom layer of the soil was frozen at all times. A snow cover is not simulated however as this would require some precipitation. Methane production was modeled by substrate dependent microbes. Their consumption and mortality had a temperature dependence given by a Q_{10} temperature response function. To provide the microbes with enough organic substrates (as in peat soils) the initial humus carbon pool was raised to $1800 kg/m$. Methane transport was modeled in a 'detailed' way. Emission and oxidation by plants was switched on, although no plant type was specified. Other parameters were left on its default value. A more complete list of the model setting and parameters is found in the appendix tables 4.2 and 4.1.

The simulated soil temperature at 15cm below the surface and methane surface flux are shown in figure 3.1. This figure can be compared with the measured data from figure 1.2. One can see that the soil temperature follows the same pattern: After a maximum in June, both the simulated and measured temperatures decrease towards the autumn with minor oscillations. During September they reach zero degree Celsius where they pause for a couple of weeks, before the layer freezes in for the winter. The methane flux in figure 3.1 follows the temperature with a little delay. A peak in temperature boosts the methane production and an emission peak follows shortly after. The subsequent increase of these peaks is not seen in nature, but suggests that a methane reservoir is build up in the soil (which was verified by inspection of these output values). At the beginning of September the soil temperatures drop below zero and the methane flux ceases. It falls exponentially through the freezing period, owing to an increase in ice blockage of the transport. Finally the methane flux drops to a value near zero, where any methane dynamics have ceased. The model did not give an effect as in the expanding membrane model (cf. 2.1).

A methane peak at the onset of freezing did not appear. There could be many reasons for this. A personal communication with Coup's developer, Per-Erik Jansson, yielded that gas bubbles in the model are assumed to freeze in and not move out during such an event. Even the permafrost bottom does not change this mechanism.

3.2 Measuring Pressure

Before the sensors were used for the experiments on the samples they were tested in trail freezing experiments.

The test measurements with the HOBO pressure sensor were very short-lived. It was placed inside a sample of water saturated peat and frozen in. The results of the test are shown in figure 4.2 in the appendix. Around the time $t = 0.2$ it shows a sharp increase in pressure, just before the pressure drops to values of below ambient atmospheric pressure ($\approx 100 kPa$) again. This is supposed to be the time when the growing ice becomes strong enough to break the sensor. From this point, the HOBO sensor never gave decent results again.

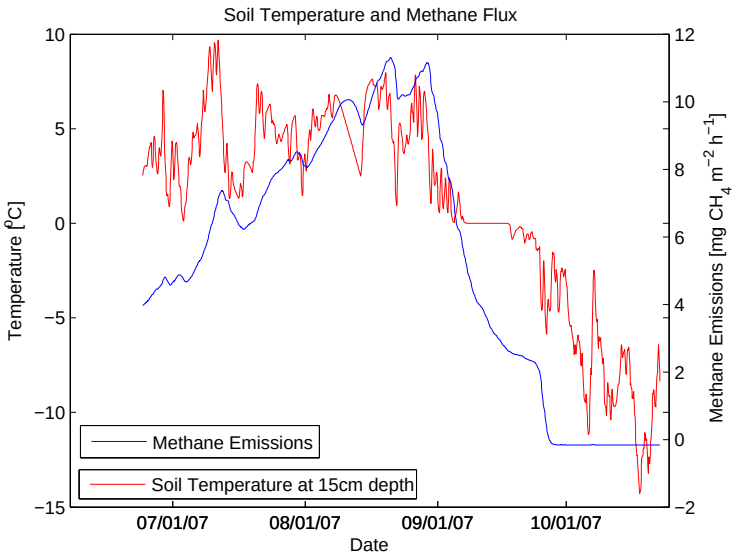

Figure 3.1: Soil temperature and methane flux as simulated by the Coup model

After the Hygrosens DS-KE-R was assembled, it was tested in freezing experiments in pure water. The sensor was placed in the middle of a plastic container (lower part of a plastic bottle) filled with roughly $80ml$ of water. This was put inside a freezer at -14^oC for about $18hrs$.

When the measurement from the bare sensor did not yield a detectable change in the signal, it was believed that amplification of the millivolt signal was necessary. Nonetheless, the ice pressure was expected to be in a detectable region without amplification, so that a problem was suspected in the transfer process of the ice pressure to the sensor membrane. Therefore different viscous substances were allocated over the membrane and the experiment was repeated.

Figure 3.2 shows the output voltage of this pressure sensor for different substances on its membrane. This is the raw signal as measured by the voltmeter on the milli-volt range, i.e. not temperature compensated or pressure calibrated. There is a distinct increase in the signal around time 0.2 if a transfer medium is used. After the maximum at time 0.4 the signal decreases again, before a slow but continuous increase sets in. It became clear that the pressure inside the solid state of water can only be measured using a transfer medium. It can however also be seen how strongly the values depend on the properties of the transfer medium. It is hard to distinguish real pressure variations from the influence of the varying transfer ability of the used substance. For the application in the peat, silicon gel was used because it probably exerts the least chemical disturbance to the sample itself.

Note how the signal of the hair wax drops into the negative range of pressure. As a matter of fact, this run of the experiment was performed after the sensor had been used in maybe 10 such runs before. During the hair wax run, the sealing of the reference cell was damaged. It became clear that improvement regarding the bonding of the cell was necessary, which was accomplished before it was used for the final experiment.

To investigate a possible hysteresis in the pressure of a freezing peat soil, the Hygrosens DS-KE-R with silicon gel was tested in a whole freeze-thaw cycle. The results of this are depicted in figure 4.4 in the appendix. A detectable hysteresis can be seen, but again it is not clear if the transfer process or actual peat soil properties are the reason for this.

The open Motorola MPX 4250 AP sensor was tested in similar experiments — and it survived the high ice pressure. Unfortunately, the results were not as reproducible as with the closed Hygrosens DS-KE-R. It was nevertheless decided to employ the sensor in the final experiment.

It is important to note that the measured pressure of the two working sensors are subject to temperature induced influence of the voltmeters and cables.

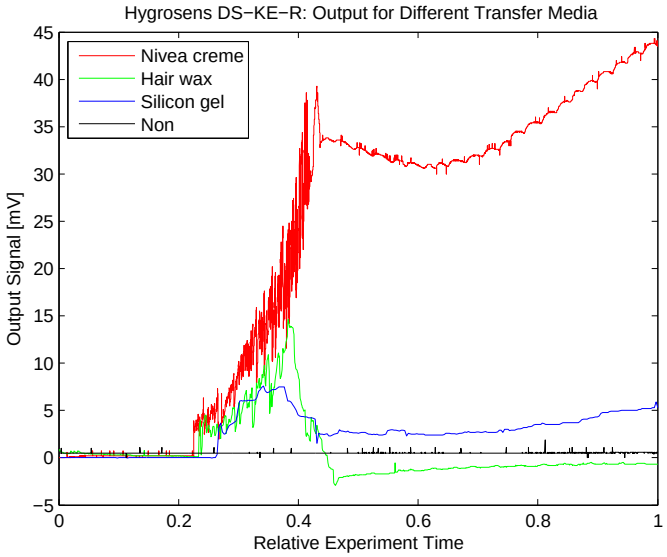

Figure 3.2: Output voltages for different transfer media as measured by a Hygrosens DS-KE-R

This means that even without the difficulties of the transfer process and a possible hysteresis, it cannot be expected to measure accurate to the kPa.

3.3 Finding a UWB Setup

In principle, microwaves were known to be able to penetrate a sample and yield information about its dielectric properties. It was therefore reckoned that UWB should be able to scan the sample's inside for these properties. It was however not known how much diffraction around the sample was to be expected. Reflections from the sample's borders and other objects in its vicinity would surely contribute to the measured signal as well. Moreover, it was not clear which antennas and frequencies would transmit a signal strong enough to be distinguished from the noise floor.

Test runs to find a working setup had to be performed. For this purpose the exact same plastic containers which contained the peat samples were filled with different trail materials. As the peat samples were expected to have a very high water content (guess was around 90%), a special focus was put on water as a trail material.

To reduce the influence of creeping waves which are diffracted around the sample, electromagnetic absorbers were available. These are made from foam which is soaked with a highly dissipative mineral. Ideally, they introduce points in space where the electromagnetic field is forced to be zero. Tests showed that the transmission through one double layer of absorbers yielded an attenuation of $-20dB$. Figure 4.5 in the appendix shows the Fourier transform of the frequencies between $7.4GHz$ and $11GHz$, for different absorber setups. The exact meaning of each peak can be argued, but the plot illustrates how the signal strength is brought down if the absorbers are cut and fitted directly on the container walls to minimize the amount of energy which is not transmitted through the sample. This practice is used to lead the main part of the transmitted energy through the sample, where it is desired.

It was also hard to estimate which form of antennas and frequency range would be best suited. It is usually assumed that such a S_{21} signal is influenced by the volume of an ellipsoid whose focus points lie at the two antennas. The width of this ellipsoid relates to the wavelength of the signal, in a way that higher frequencies have a narrower ellipsoid than lower frequencies. For the experiment here, this scanned volume should be as small as possible in order to get the highest possible resolution in space. On the other hand, higher frequencies are attenuated more strongly in general, and in water in the lower GHz region (cf. Debye plot 2.3) in particular. To still see the transmitted signal, a compromise is needed.

Typically, antennas do not radiate plane waves but somewhat spherically shaped wave fronts. It was tried to focus a beam of $7.4GHz$ to $11GHz$ using horn antennas, a time domain plot of which is seen in figure 4.6. One can see how the free space signal arrives fastest, closely followed by a transmission through rapeseed oil (rapsolja) and water. As water has a real part value of its relative permittivity of around 80, one would expect the transmission peak through $30cm$ at roughly $\sqrt{80}ns$ after the free space peak. This is not at all what was measured, so that one is led to believe that the largest part of the energy travels around the sample to the receiver. This increase of its path length corresponds well to the measured time delay of the signal. On the other hand, the signal through rapeseed oil which has a real value of the dielectric permittivity around 3, did not diffract heavily around the box. Consequently, the actual transmission was detected and the permittivity of rapeseed oil could be calculated. This demonstrates how much simpler the measurements get for only sightly dielectric materials.

It became clear that lower frequencies had to be used in order to measure a sample containing loads of water. For decreasing frequencies horn antennas grow in their size, so that they would become bigger than the samples. One could therefore not make use of them.

A working setup was found from 0.8 to $3.3GHz$ with so-called Skycross antennas. In order to focus the beam a little wave guide was build. That is to say that the antennas were not placed directly on the container, but some $10cm$ away. The created channel was shielded by absorbers, so that the waves entering the peat sample were a little more plane that originally emitted. Figure 4.7 shows a comparison of the values that were attained with this setup and the theoretical values as simulated by Debye theory.

The final setup is sketched in 2.4. Sweeping once over the 1601 frequencies which were measured for both S_{21} and S_{11} took roughly a minute. This gave the time resolution of the measurement.

3.4 Two Freezing Experiments

After the samples incubated for a month, the gas analyzer was working, the temperature and pressure sensors were assambled, the UWB method was set up and the freezer was turned up-side-down, two freezing experiments were conducted. As the temperature and pressure sensors together with their cables were expected to interfere strongly with the microwaves of the UWB method, it was decided to apply the methods separately. On the first sample the gas flux, temperature field and pressure variations were measured. In the second run only the gas flux and microwave response was measured. In comparison with the first run, the second run imposed a lot less disturbance upon the sample. Table 3.1 shows an overview over the final freezing experiments which were conducted.

During the first run the sample was subjected to a temperature of roughly -18^oC from above for the first week of the experiment. At the end of day seven the freezer was switched off and the room temperature gradually increased to $+20^oC$ again. Figure 3.3 shows the development of the temperature profile during the experiment. Note how the soil layers freeze in the desired manner, i.e. starting from the top, proceeding to the bottom. The thawing was not the primary subject of this investigation which is why it was not waited until the entire sample was at above zero temperatures again.

The methane emissions from the sample are plotted in figure 3.4. One can see a rather constant flux which is superimposed by oscillations caused by the varying room temperature. The white line on top of the emission data shows an hourly average of the flux. The vertical black line at the end of day seven marks the freezing-thawing interface. The methane emissions do not exceed $20mgCH_4m^{-2}h^{-1}$ at any time of the experiment. This means that the emissions from the sample are well inside the noise floor. The amplitude of the noisy oscillations is almost $10mgCH_4m^{-2}h^{-1}$. In comparison with the Zackenberg measurements (cf. 1.2) this baseline of fluctuations is rather large. Note however that the Zackenberg measurements are the result of an average over six chambers, which reduces the noise background.

The two working pressure sensors were implanted at equal heights into the water saturated part of the sample, at about $5cm$ below the water table. Figure 3.5 shows the soil temperature at the position of the pressure sensors, and their calibrated as well as temperature-compensated output. The temperature compensation accounts for thermal variations of the reference pressure in the sensor's gas cell according to the ideal gas law, equation (2.5).

The open pressure sensor (red line) shows an increase until day 3. Then it stays a little above the ambient atmospheric pressure of around $100kPa$ over

Run	1	2
Measured Variables	Gas Flux, Pressure, Temperature	Gas Flux, Microwave response (0.8 to 3.3GHz)
Incubation time	5 weeks	7 weeks
Weight	19.5kg	16.7kg
Water table	11cm	16.5cm

Table 3.1: Overview of the experimental parameters of the two runs

the entire time of the experiment. Any occurrence of an overpressure was not transferred to the measuring membrane or must immediately have been released via the open end of the sensor's tube. Perhaps a bit of ice froze in the tube and shielded the gas in the sensor from the outside pressure. As a matter of fact, the same could occur for real bubbles in freezing peat. The constant signal opposes some results from test runs performed with this sensor, but is somehow in agreement with the constant methane flux which was observed.

The closed pressure sensor was used with silicon gel as a transfer medium. This rubber-like medium transfers only a part of the pressure to the membrane. And as the viscosity of the gel depends on the temperature, the pressure is not transferred equally at all times. The superposition of this effect makes it hard to read off the actual pressure of a sealed bubble in a freezing peat soil. The pressure starts just below 115kPa which is a reasonable value considering the water head on top of it. The variations until day five might stem from the transfer medium, they might also demonstrate effects of cryogenic suction towards the freezing front. One can see a distinct increase at day five when the phase transition at this height of the sample is completed. The pressure increases to over 170kPa, but the fact that it decreases even before the thawing sets in shows how the transfer capability of the silicon gel decreased with temperature. The real pressure might very well have been an order of magnitude higher than measured here. The slope of the large peak at the onset of thawing gives an idea of what the pressure might have been before the thawing.

The second run was used to check the feasibility of ultra-wideband spectroscopy. The peat sample can be regarded as undisturbed as nothing was implanted into it. The chamber on its top captured the methane flux, two antennas outside the container measured electromagnetic signals. The freezer and the rest of the setup was identical to the first run, so that the temperature distribution can be assumed to follow approximately the same pattern in both cases. The abovementioned mapping of the temperature data of run one and two by the means of the methane peak could however not be executed.

Figure 3.6 shows the methane emissions over the entire experiment. The vertical black line marks the point in time at which the freezer was removed and the thawing initiated. Again, the white line on top of the flux data is an hourly average of the emissions. One can see the same baseline of fluctuations as in the first run. At the onset of thawing however, a set of sharp peaks in the methane emissions were detected — the highest of them at almost 300$mgCH_4m^{-2}h^{-1}$. These peaks came as a major surprise, at a time where the experiment was already believed to be over. The first of this bursts occurs just 2 hours after the freezing process was stopped. The center of the set of peak lies about 16 hours after the onset of thawing. When these dynamics have ceased (day 10), the emissions fall back to their base line. The interesting time span is shown in more detail in figure 4.8 in the appendix.

The emission pattern shows a certain similarity to the Zackenberg data of 2007: Very high emissions on a small base line of methane production, at a time when the water is changing its phase, and frost action is in progress. In this experiment however, there is further information available which helps to find the underlying reason.

Figure 3.7 depicts the transmitted signal, S_{21}, in frequency space after calibration. At the first glance, one sees how the received strength of the signals increases during the freezing period (day 2 to 8) before it decreases again during thawing. This is in accordance with the expectation as ice attenuates the waves a lot less than water. In general higher frequencies (here plotted at the bottom) have more attenuation than the lower ones. What is a little unexpected however, is the dip of amplitude between 1 and 1.5GHz. One explanation for this could be the increase in the bound water fraction as the soil

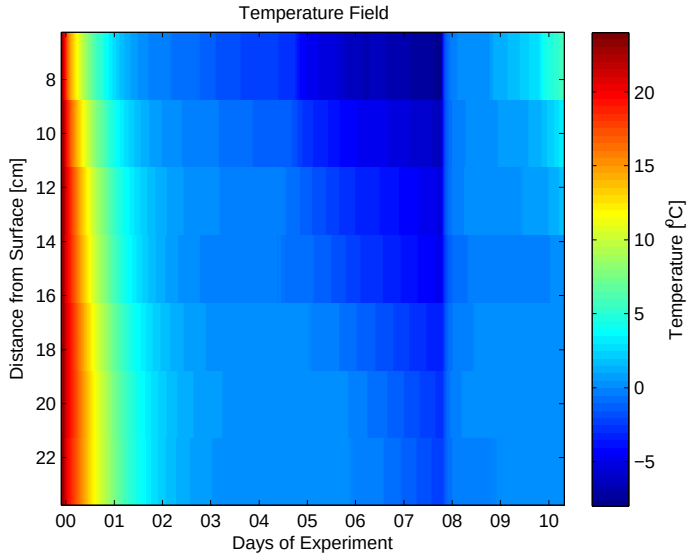

Figure 3.3: Soil temperatures as measured by the array of seven sensors (run 1)

freezes, because these molecules have a lower relaxation frequency than free water molecules (cf. section 2.2.5).

The same signal is shown in the time domain in figure 3.8. Here one can see how the signal tends to arrive earlier as the water content goes down during freezing. At day seven there is a nice periodicity in the arrival of transmission peak. This is interpreted as re-bouncing waves between the container walls.

To further investigate the gas dynamics, the frequency range from 2.3 to $3.3GHz$ was chosen and only the time interval around the freeze-thaw interface was regarded. A plot of these uncalibrated signals is see in figure 3.9. All lines come in rather steadily at day 7.6. The fact that they are still increasing a little suggests that the sample was not totally frozen yet, i.e. not in exact equilibrium with its thermal environment. As the amplitude goes down again during thawing, one can see small, sudden jumps in each of the frequency lines. Because the overlaying thawing process occurs on larger time scales, one is let to believe that these deflections could be caused by rapid changes in the sample, like sudden gas redistributions.

To investigate this further, the measured methane flux was compared to the average time derivative of the amplitudes of these frequencies. Both of these signals were normalized to their maximum and plotted together. The result of this is shown in figure 3.10. The similar plot 3.11 shows the average derivative of the angle and methane emission, this time in more detail. The accordance of both signals is amazing. Typically, a positive change in S_{21} is followed by a methane release one minute later. The only exception to this is at time $8.1days$ where a positive change of the transmission does not entail a methane peak. Considering the challenge of free space measurements in general, and the difficulties of the applied setup in particular, this constitutes a stunning result of the performed work. It was unsure at the beginning if any gas dynamics of the sample could really be captured in a UWB signal, and here one can resolute individual gas bursts. Note however, that although all clocks were synchronized, a single measurement takes each of the method about one minute, so that an error of about one minute is imposed to the time scale.

In order to translate this relation to actual gas dynamics, ε had to be calculated. As mentioned above, this implies a grid search which has to be done for all frequency and time points. This is highly computation-intensive, so that a proper evaluation of the whole experiment would take several weeks. The decision was made to only look at the interesting time around the onset of thawing. The university computation cluster $LUNARC$ was employed to perform the job. The results are shown in figures 3.12 and 3.13. One can see how the relatively stable values

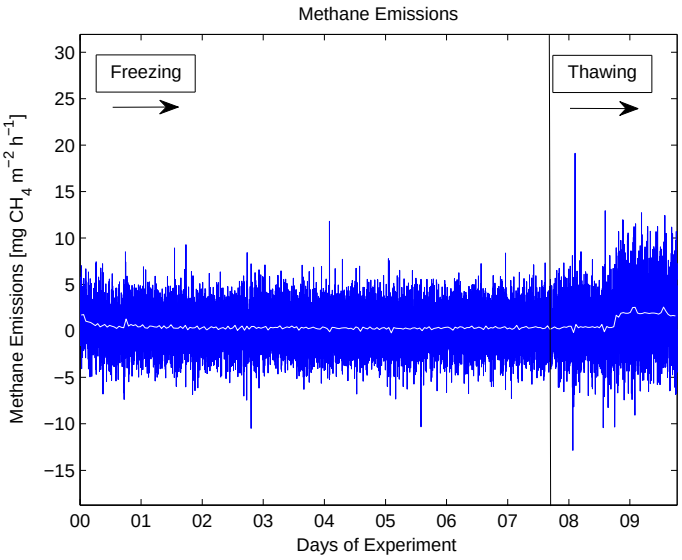

Figure 3.4: Soil emissions of methane (run 1)

before the onset of thawing (day 7.8) evolve while the sample thaws. Regarding the real part, the transition over time (along horizontal axis) is stronger in the region below $2.2GHz$. Higher frequencies are subject to slower variations, which is why they were chosen to investigate the sudden changes due to gas bursts. In the imaginary part one finds a valley of lower attenuation along the frequency of $2GHz$.

The result of the three material mixing model is seen in figure 3.14. The vertical black indicates when the freezing was stopped. From there on the mixing model yields a steady decrease of the solid material's volume (blue line). Equally, the volumetric water content increases again — plausible for a thawing process. As these results were attained without further input of information, one is led to believe that this simple mixing model cannot be too far off reality. These general trends are superimposed by smaller variations, dominantly in the solid and gas content. The large fluctuation at time $8.1days$ seems counter intuitive. It corresponds to the abovementioned inconsistency between S_{21} and the methane emissions. It can be speculated that this is due to internal gas dynamics which did not reach the surface. There might also be gases which did not contain any methane.

Finally, figure 3.15 shows the change of the three volumetric fractions through time. This excerpt depicts an interval of about $7hours$ during the thawing process. The dips in the derivative of the gas content are the direct consequence of change in the measured S_{21} signal and therefore match with the methane emissions, just like in figure 3.11. After all, this was the ultimate goal for this part of the experiment.

Further runs were originally planned for the project. These include the measurement on a sample which has not been incubating at high temperature and humidity. This was supposed to yield information about the impact of the accumulated methane reservoir in the sample. It also seems dispensable as there is still so much data left to analyze: In the whole evaluation of the microwave signal the reflection, S_{11}, was not even looked at. That alone has a potential for a major improvement of the results. There are also a lot of other issues regarding the experiment design which should be reconsidered before further runs are performed.

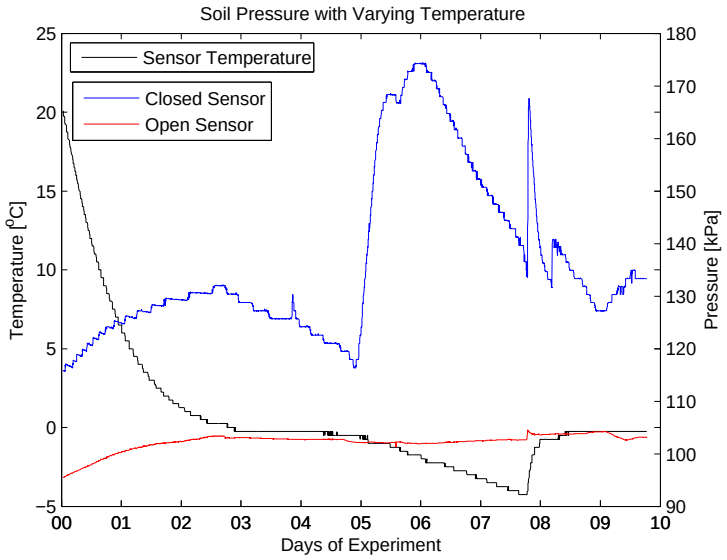

Figure 3.5: Pressure and temperature as measured by the two different sensors (run 1)

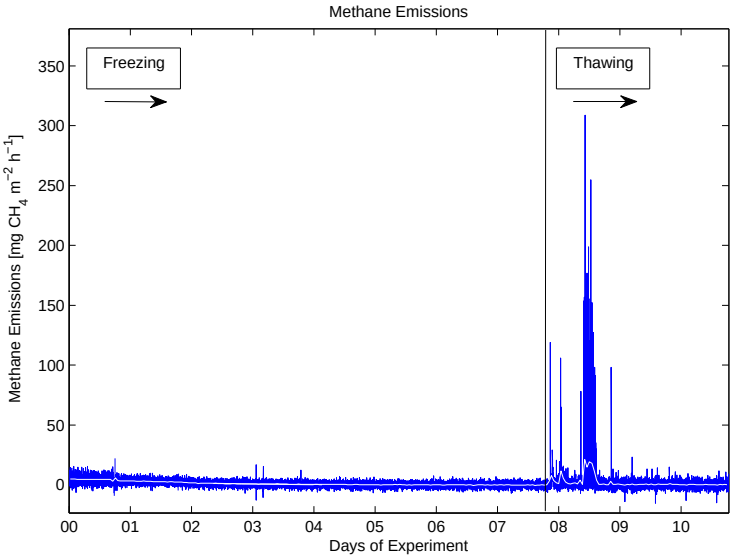

Figure 3.6: Methane emissions with the hourly average as white line (run 2)

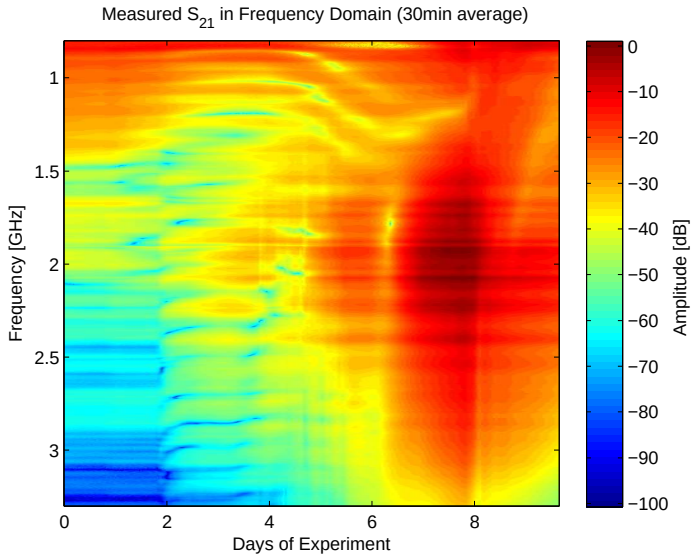

Figure 3.7: Measured S_{21} transmission in the frequency domain

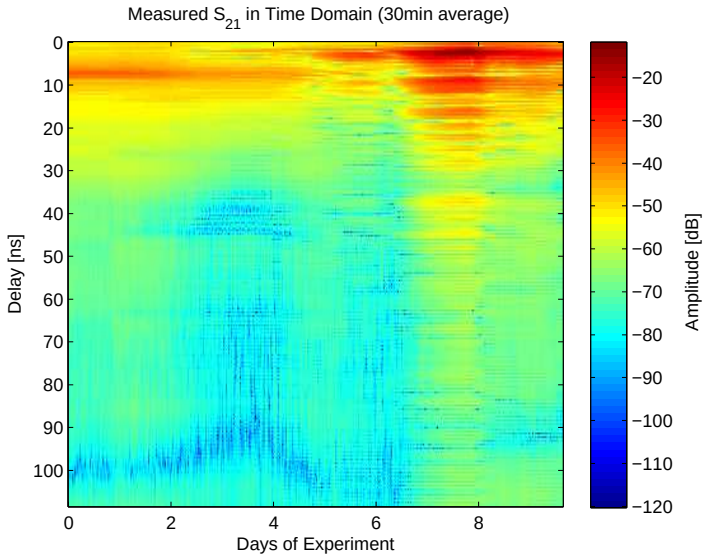

Figure 3.8: Measured S_{21} transmission in the time domain

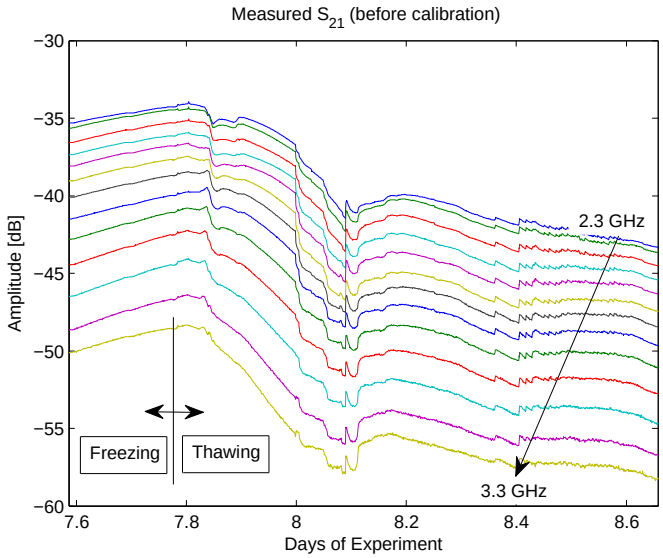

Figure 3.9: Measured S_{21} transmission before calibration around the freeze-thaw interface for the frequencies used in further analysis in relation to methane dynamics

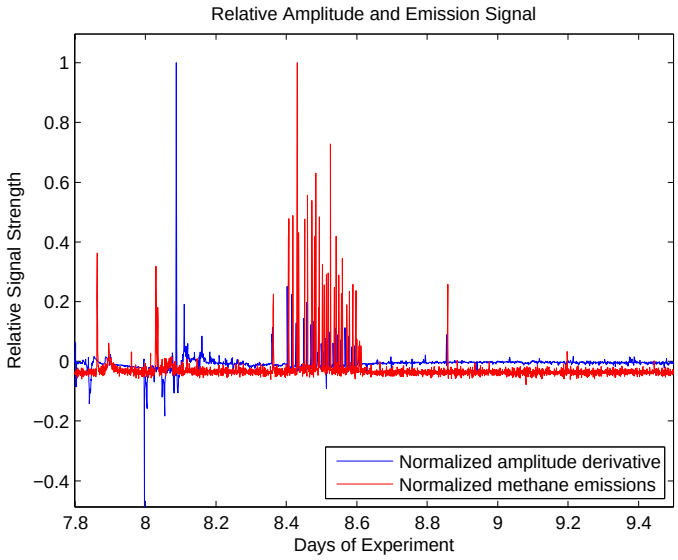

Figure 3.10: Normalized amplitude of transmission and methane emissions for a part of the thawing period

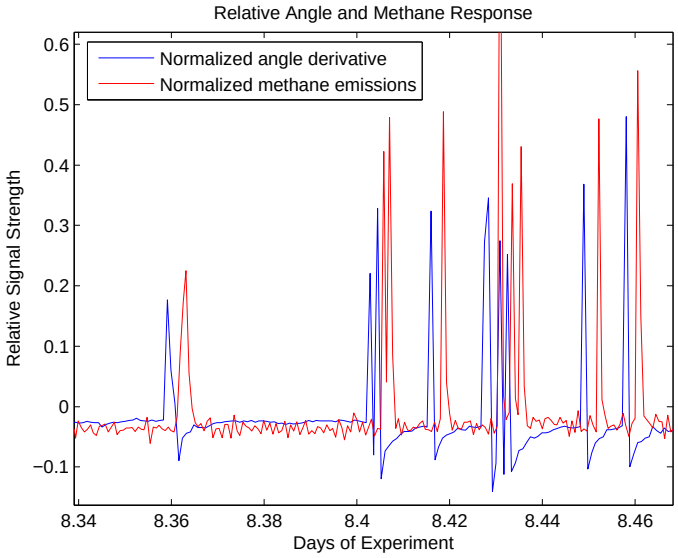

Figure 3.11: Normalized angle of transmission and methane emissions for a part of the thawing period

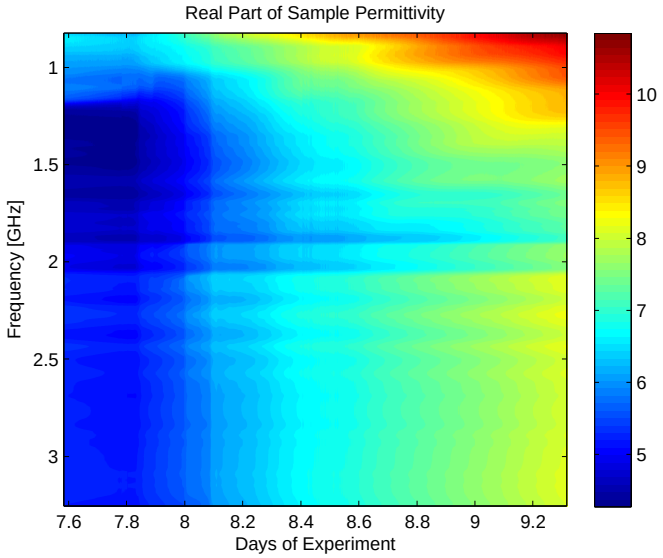

Figure 3.12: Calculated real part of the dielectric permittivity for times around the freeze-thaw interface

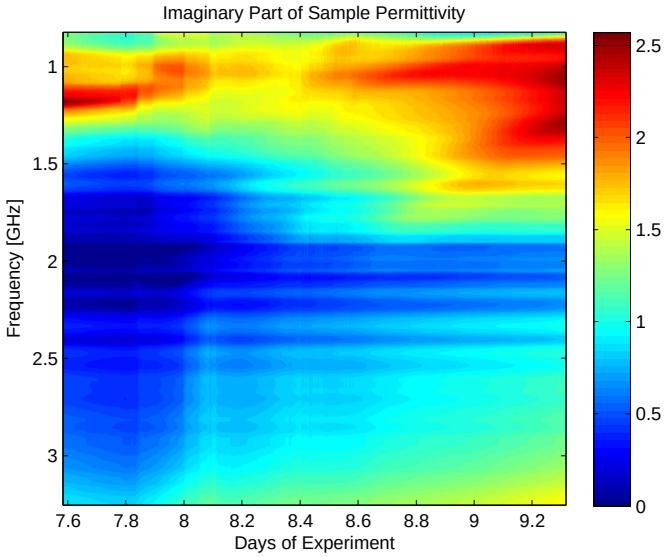

Figure 3.13: Calculated imaginary part of the dielectric permittivity for times around the freeze-thaw interface

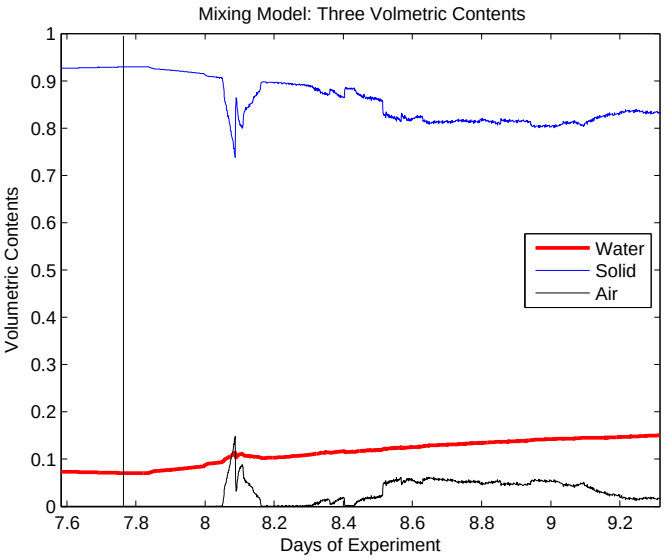

Figure 3.14: Results of the three-material mixing model for times around the freeze-thaw interface (marked by vertical black line)

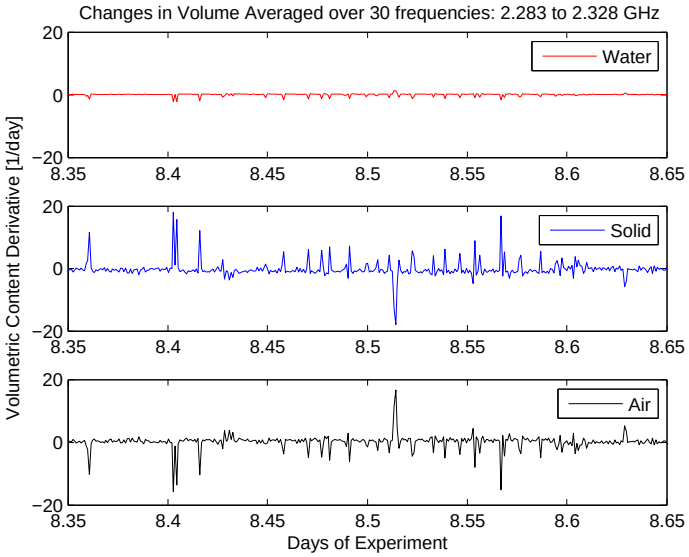

Figure 3.15: Time derivative of the three volumetric contents for times around the freeze-thaw interface

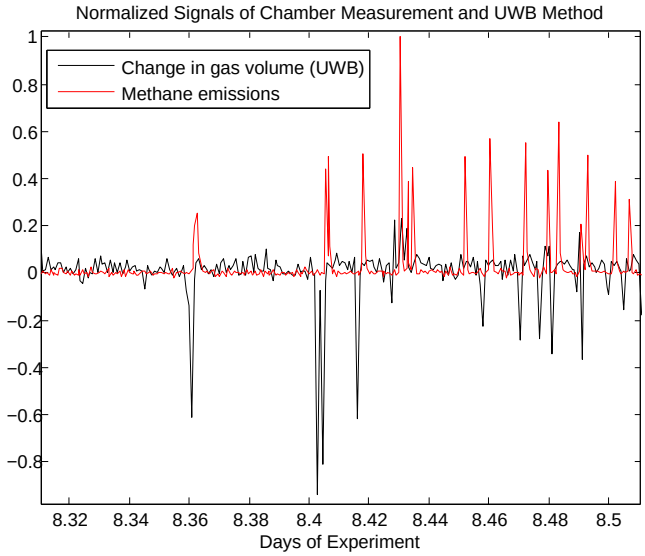

Figure 3.16: A final comparison of the two approaches

Chapter 4

Conclusions

A SVAT model simulation was performed driven by measured climate data from the Zackenberg Research Station, so that it can be compared with the measurements from figure 1.2.

The model was in principle able to simulate the methane surface flux, with some of the characteristics of the measured emissions. The model run did however not predict a methane burst at the onset of freezing.

This does nevertheless not mean that the methane emission peak is excluded by theory. Although SVAT models are based upon the physical principles described in section 2.1, they simplify and generalize the contributing processes. This includes material parameters which are assumed constant, response functions which are idealized and so forth. These parameters describe collective effects and are inherently necessary for the model because it does not work on an atomic scale.

A new mechanism is needed to incorporate the methane burst at the onset of freezing into SVAT models. The formulation of this mechanism requires certainty about the reason for the emission peak first. Once the driving force of the process is found, this mechanism must be linked to the other parts of the model. The principle of finite element solving however remains unaffected.

For the reproduction of the natural conditions of soil freezing in the laboratory, a working setup was found which froze the sample in the desired manner. The most effective cooling mechanism was a freezing box around the top of the sample.

The exact right conditions of Greenland were however found very hard to realize. This was partly because the *right* natural conditions were not even known, and partly because heat fluxes are generally hard to control exactly. In nature the permafrost bottom might induce a trace of a two-sided freezing of the active layer. This has not been incorporated in the experiments.

The freezing setup can be further optimized. A constant build-up of ice in the gas tubes had a tendency to cause a blockage, for example. To avoid this, heated gas tubes could be designed.

The scale of time and space in the laboratory are inherently different from nature, with consequences that are hard to estimate. The freezing in the laboratory was rather fast compared to nature. Some properties of ice depend on the freezing rate, and maybe one of these properties is of vital importance for the methane peak. For this experiment it was decided to freeze the samples unnaturally fast in order to minimize the heat fluxes from the sides of the containers. This ensured the desired top-down freezing, but might have cost the *right* ice properties.

These problems can be circumvented by in situ monitoring. The Zackenberg emissions measured in 2008 for example, do not show the methane burst at the onset of freezing. Further field site measurements are needed to single out the decisive variables.

The main result of the methane flux measurements is that the peak in emissions does not occur when the soil is continuously frozen in.

The first run of the freezing experiment did not show any significant methane emission events. Considering the fact that not even a minor peak was measured during the steady freezing, one is led to believe that there must be a fundamental difference to nature when the methane burst occurs. This could be related to the inadequate freezing as described above. It might also relate to an insufficient incubation time. The samples frozen in this experiment were given just over a month to incubate methane. Although the conditions in nature are not specially made for

methane production, the soil is given an entire summer to accumulate methane.

After the second run however, it was found that a substantial amount of methane is emitted at the onset of thawing. The significance and immediacy of the response to the changed ambient temperature suggests the release of a methane storage. The emission peaks occurred at times when large parts (around 90 %) of the sample were still frozen in. Methane production of this strength is very unlikely. Such a release of a methane reservoir might be based upon a mechanism which is related to the occurrence of the Greenland peak. The similarities of their occurrence can be used to single out the underlying reason.

A large part of the problems with the methane measurement relate to the actual methane detection: The photo-acoustic method of the gas analyzer carries a temperature dependence. Although the experiment was conducted in a so-called constant room, one picks up some temperature related noise in the methane signal. Furthermore, the methane measurements are affected by humidity variations as well as carbon dioxide concentration variations. There is a possibility to remove these influences by a use of chemicals, but even then it is important to minimize temperature variations. Another way of improving the measurement is to employ a different detection method, e.g. gas chromatography.

The techniques of sub-surface pressure sensing yielded a pressure increase at freezing. These results were attained from industrial pressure sensors which were modified for the purpose of measuring gas bubble pressure in freezing soils. The output data of pressure sensors is very much dependent on their working mechanism. The geometrical design as well as the used transfer medium have a tremendous impact on the measurements. This goes so far that a lot of the variability seen during freezing experiments are direct consequences of the inner structure of the transfer medium. This influence must be kept minimal to find a correlation of the pressure to the gas flux.

Another problem was to even find the right range for the sensor. More testing about this and the transfer media should be conducted in the future. The method needs further improvement before it can be used as a reliable way of measurement.

It is moreover obvious that the implementation of the sensors into the peat is very invasive. No gas peaks at the onset of thawing were detected from the respective peat sample. This suggests that they were squeezed out during the implementation of the sensors. That in turn can hardly be eliminated for such an experiment. If such a method is applied, it is of utmost importance for the gas dynamics to insert the sensors a sufficiently long time before the freezing to not disturb the sample after it has produced its methane reservoir.

The samples were taken, stored and frozen inside plastic containers in order to have the possibility of transmitting radiowaves through them. The flexibility of the container walls might have been too high for the required pressure for the methane burst.

Ultra-wideband spectroscopy was able to track gas dynamics inside a freezing peat soil. Not only could the gas bursts be reliably detected, but also could the composition of the soil be determined. Individual bursts could be resolved and their effect on the sample's composition could be estimated by a dielectric mixing model. The results of the change in volumetric contents (cf. figure 3.15) show that the loss of gas volume during a methane burst is compensated by an increase in soild volume, i.e. ice or peat. This supports the theory of a squeezing out of gases. It does however not explain the mechanism of the methane burst. A long term application of this method in the field has the potential of yielding incredible new insights into soil physics and methane dynamics.

The field for improvements of the setup is immense, but the feasibility of the current setup could impressively be demonstrated here. Antennas, amplifiers, sample dimension and post-processing are just some of the aspects at which compromises were made.

It might have been harder to filter out gas bursts from the UWB signal at the onset of freezing because the signal carried a lot more variations at this time. Further testing is needed to overcome this difficulty.

In order to get more experience as to how gas bubbles influence a UWB signal, trail experiments should be performed in which bubbles are artificially inserted into a peat sample or a highly viscous medium. Once it is better understood how a passing bubble looks like in the microwave response, the interpretation of the actual data becomes more reliable.

Despite all problems and uncertainties it can be summarized that methane bursts from peat soils in connection with frost action could be detected.

From the first run of the experiments conducted

here, it is clear that the pressure increases significantly at soil freezing. At the onset of thawing there is still a considerable overpressure in closed gas bubbles. As soon as the first bits of ice melt, this pressure results in a gas discharge through the sample's surface.

It could be speculated that the methane burst from Zackenberg 2007 was the consequence of a series of small thawing events which were superimposed to the general freezing trend. A steady freezing did not give a peak under laboratory conditions, and perhaps it would not give one in nature either.

It seems as if the methane burst is more complicated than originally believed. The series of experiments conducted here are valuable, as their results have similar characteristics as the methane burst in nature. Field work however can not be made up for in the laboratory.

The present work demonstrates three independent methods with the potential to explain the methane peak at the onset of freezing. It seems as if UWB has the most potential of capturing the peak. This of course requires a peak to come at the onset of freezing, and also does not give an immediate answer to the reason of the 2007 Zackenberg observations.

Acknowledgments

I would like to gratefully thank my supervisor Torben Christensen. His advice, enthusiasm and support was of vital importance as to all my work. Thanks to Mikhail Mastepanov who kindly helped to solve all kinds of problems, from sampling peat in a bog to turning over freezers. The UWB part of this project would not have been possible without the assistance of the Department of Electrical and Information Technology — first and foremost Telmo Santos, Anders J. Johansson and Fredrik Tufvesson. My greatest thanks to you. A special thank you to my father who helped with words and deeds establishing the pressure measurement and assembling its electric circuits. Thanks to Carl-Erik Magnusson for taking care of the organizational issues related to the cooperation of the different departments. Finally, I would like to say thank you to all friends for supporting and enduring me during my project.

References

[Bergmann et al., 1992] Bergmann, H., Mischke, B., Scholz, U., and Schoppnies, E. (1992). *Lexikon der Sensortechnik*. vde-Verl. Berlin.

[Brovelli and Cassiani, 2008] Brovelli, A. and Cassiani, G. (2008). Effective permittivity of porous media: a critical analysis of the complex refractive index model. *Geophysical Prospecting*, 56(5):715–727.

[Clymo et al., 1998] Clymo, R., Turunen, J., and Tolonen, K. (1998). Carbon accumulation in peatland. *Oikos*, 81(2):368.

[Comas and Slater, 2007] Comas, X. and Slater, L. (2007). Evolution of biogenic gases in peat blocks inferred from noninvasive dielectric permittivity measurements. *Water Resources Research*, 43(5):W05424.

[Gorham, 1991] Gorham, E. (1991). Northern peatlands: role in the carbon cycle and probable responses to climatic warming. *Ecological Applications*, pages 182–195.

[Håkansson et al., 2007] Håkansson, E., Amiet, A., and Kaynak, A. (2007). Dielectric characterization of conducting textiles using free space transmission measurements: Accuracy and methods for improvement. *Synthetic Metals*.

[Hallikainen et al., 1985] Hallikainen, M., Ulaby, F., Dobson, M., El-Rayes, M., and Wu, L. (1985). Microwave dielectric behavior of wet soil-Part 1: Empirical models and experimental observations. *IEEE Transactions on Geoscience and Remote Sensing*, pages 25–34.

[Hansson et al., 2004] Hansson, K., Simunek, J., Mizoguchi, M., Lundin, L., and Van Genuchten, M. (2004). Water Flow and Heat Transport in Frozen Soil Numerical Solution and Freeze-Thaw Applications. *Vadose Zone Journal*, 3(2):693–704.

[Hartikainen and Mikkola, 2001] Hartikainen, J. and Mikkola, M. (2001). Numerical Solution of Soil Freezing Problem by a New Finite Element Scheme. *SOLID MECHANICS AND ITS APPLICATIONS*, 87:61–66.

[Hillel, 1998] Hillel, D. (1998). *Environmental soil physics*. Academic press.

[Huisman et al., 2003] Huisman, J., Hubbard, S., Redman, J., and Annan, A. (2003). Measuring Soil Water Content with Ground Penetrating Radar A Review. *Vadose Zone Journal*, 2(4):476–491.

[Hurd et al., 1962] Hurd, R., Schmid, G., and Snavely, E. (1962). Electrostatic Fields: Their Effect on the Surface Tension of Aqueous Salt Solutions.

[Jiang and Wu, 2004] Jiang, J. and Wu, D. (2004). Ice and water permittivities for millimeter and sub-millimeter remote sensing applications. *Atmospheric Science Letters*, 5(7).

[Kellner et al., 2004] Kellner, E., Price, J., and Waddington, J. (2004). Pressure variations in peat as a result of gas bubble dynamics. *Hydrological Processes*, 18(13).

[Kettridge and Binley, 2008] Kettridge, N. and Binley, A. (2008). X-ray computed tomography of peat soils: measuring gas content and peat structure. *Hydrological Processes*, 22(25).

[King and Fletcher, 1973] King, W. and Fletcher, N. (1973). Pressures and stresses in freezing water drops. *Journal of Physics D Applied Physics*, 6(18):2157–2173.

[Lelieveld et al., 1998] Lelieveld, J., Crutzen, P., and Dentener, F. (1998). Changing concentration, lifetime and climate forcing of atmospheric methane. *Tellus B*, 50(2):128–150.

[Lichtenecker, 1926] Lichtenecker, K. (1926). Dielectric constant of natural and synthetic mixtures. *Phys. Z*, 27:115.

[Lin, 2003] Lin, C. (2003). Frequency domain versus travel time analyses of TDR waveforms for soil moisture measurements. *Soil Science Society of America Journal*, 67(3):720–729.

[Mastepanov et al., 2008] Mastepanov, M., Sigsgaard, C., Dlugokencky, E., Houweling, S., Ström, L., Tamstorf, M., and Christensen, T. (2008). Large tundra methane burst during onset of freezing. *Nature*, 456(7222):628–630.

[Matthews and Fung, 1987] Matthews, E. and Fung, I. (1987). Methane emission from natural wetlands: Global distribution, area, and environmental characteristics of sources. *Global Biogeochemical Cycles*, 1(1).

[Michalowski and Zhu, 2007] Michalowski, R. and Zhu, M. (2007). Freezing and Ice Growth in Frost-Susceptible Soils. *SOLID MECHANICS AND ITS APPLICATIONS*, 146:429.

[Mikaloff Fletcher et al., 2004] Mikaloff Fletcher, S., Tans, P., Bruhwiler, L., Miller, J., and Heimann, M. (2004). CH4 sources estimated from atmospheric observations of CH4 and its I3C/I2C isotopic ratios: 2. Inverse modeling of CH4 fluxes from geographical regions. *Global Biogeochem. Cycles, 18 (4)*.

[Moore and Knowles, 1990] Moore, T. and Knowles, R. (1990). Methane emissions from fen, bog and swamp peatlands in Quebec. *Biogeochemistry*, 11(1):45–61.

[Potter, 1973] Potter, D. (1973). *Computational Physics*. John Wiley and Sons Ltd.

[Richter, 1987] Richter, J. (1987). *The soil as a reactor: modelling processes in the soil*. Catena.

[Schwarzel et al., 2006] Schwarzel, K., Simunek, J., Stoffregen, H., Wessolek, G., and Van Genuchten, M. (2006). Estimation of the Unsaturated Hydraulic Conductivity of Peat Soils Laboratory versus Field Data. *Vadose Zone Journal*, 5(2):628–640.

[Sigunov and Samylova, 2006] Sigunov, Y. and Samylova, Y. (2006). Pressure growth dynamics during freezing of a closed volume of water with dissolved gases. *Journal of Applied Mechanics and Technical Physics*, 47(6):842–848.

[Torrance and Schellekens, 2006] Torrance, J. and Schellekens, F. (2006). Chemical factors in soil freezing and frost heave. *Polar Record*, 42(01):33–42.

[Walter and Heimann, 2000] Walter, B. and Heimann, M. (2000). A process-based, climate-sensitive model to derive methane emissions from natural wetlands: Application to five wetland sites, sensitivity to model parameters, and climate. *Global Biogeochemical Cycles*, 14(3).

[Wensink, 1993] Wensink, W. (1993). DIELECTRIC PROPERTIES OF WET SOILS IN THE FREQUENCY RANGE 1-3000 MHz 1. *Geophysical Prospecting*, 41(6):671–696.

[Whiting and Chanton, 2001] Whiting, G. and Chanton, J. (2001). Greenhouse carbon balance of wetlands: methane emission versus carbon sequestration. *Tellus B*, 53(5):521–528.

[Zakri et al., 1998] Zakri, T., Laurent, J., and Vauclin, M. (1998). Theoretical evidence for'Lichtenecker's mixture formulae'based on the effective medium theory. *JOURNAL OF PHYSICS-LONDON-D APPLIED PHYSICS*, 31:1589–1594.

Appendix

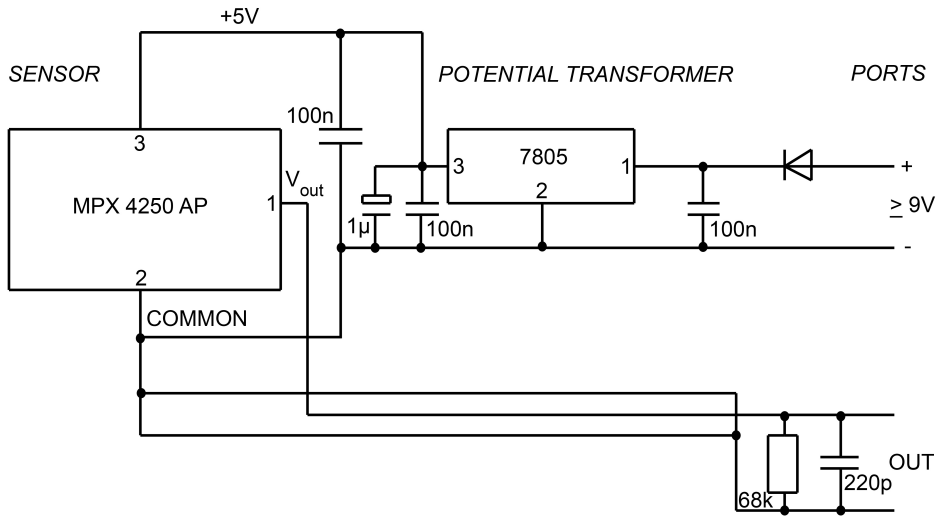

Figure 4.1: Electric circuit of the Motorola MPX4250 AP with a 7805 voltage regulator

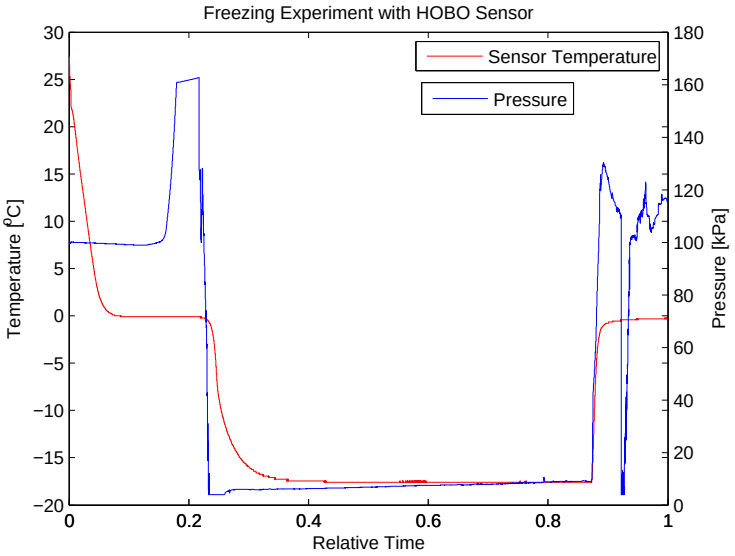

Figure 4.2: A freezing cycle as measured by a HOBO U20-001-01

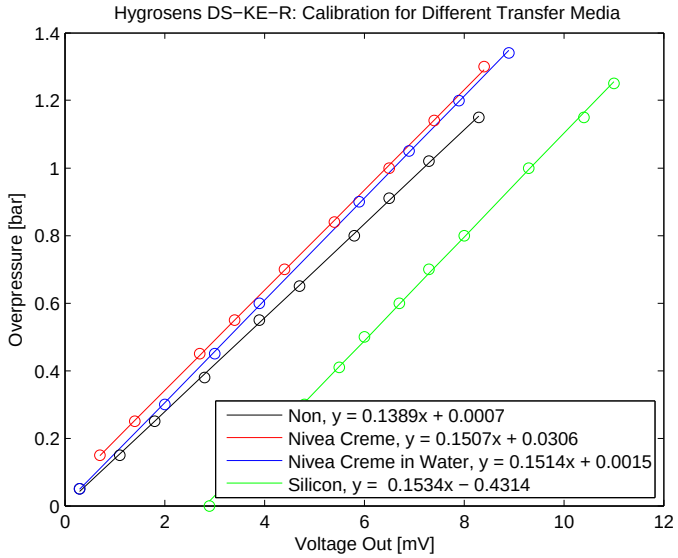

Figure 4.3: Pressure calibration curves for different transfer media on a Hygrosens DS-KE-R

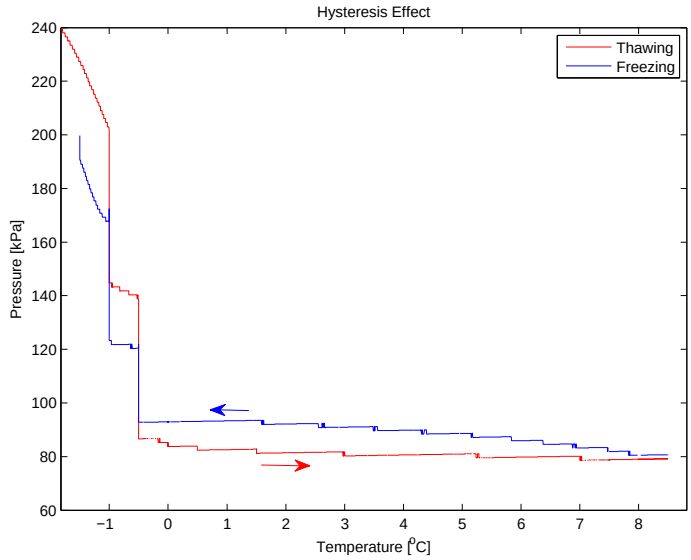

Figure 4.4: Hysteresis effect of the freezing cycle as measured by a Hygrosens DS-KE-R

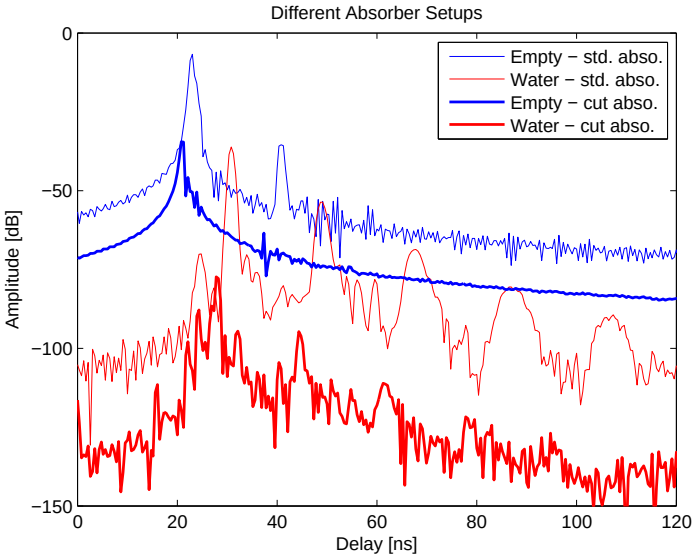

Figure 4.5: Influence of different absorbers on the transmitted signal in the time domain

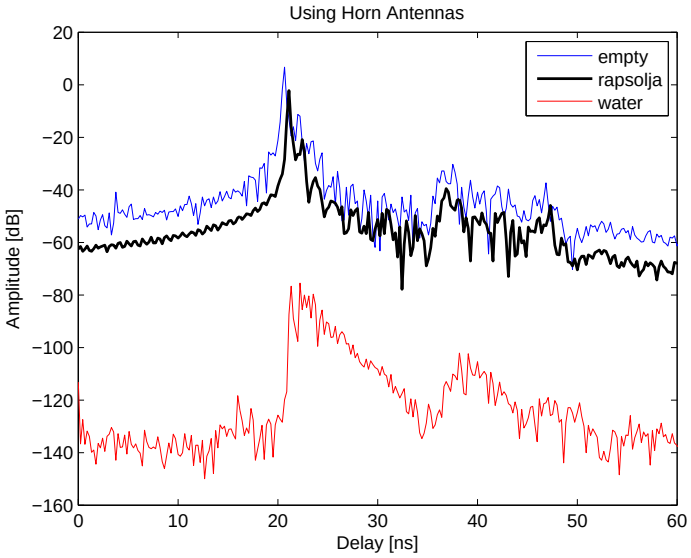

Figure 4.6: Transmitted signal of two horn antennas for different materials

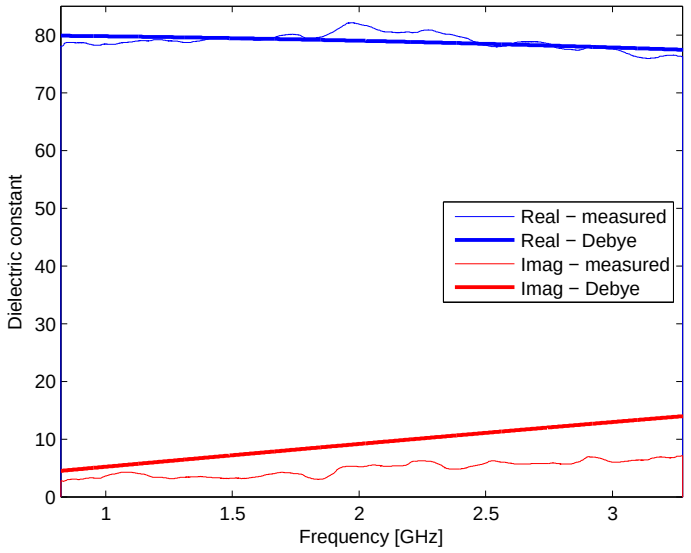

Figure 4.7: Theoretical prediction versus measured value with Skycross antennas

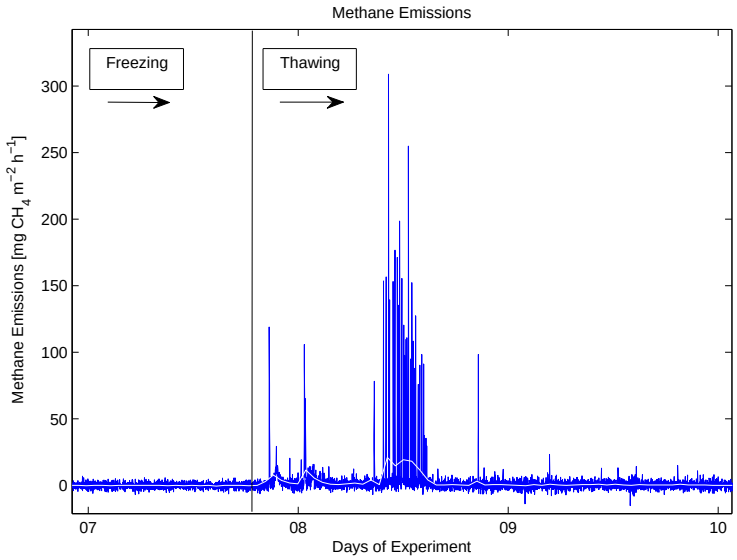

Figure 4.8: Methane emissions in more detail (run 2)

Table 4.1: CoupModel parameters for the methane flux simulation

Parameter	Value	Unit
Common abiotic responses		
TemQ10	3.5	-
TemQ10Bas	20	C
Meteorological Data		
HumRelMean	70	percent
ReferenceHeight	2	m
Slope E-W	0	m/m
Slope N-S	0	m/m
WindspeedMean	2	m/s
Soil organic processes		
CN Ratio Microbe	10	-
Eff Microbes	0.5	1/day
Eff humus	0.5	1/day
Init H CTot	180000	g/m
Init H Depth	-1	m
Init L1 CTot	50	g/m
Init L1 Depth	-1	m
Init L1 NTot	10	g/m
Init M CTot	10	g/m
Init M Depth	-1	m
Init M NTot	10	g/m
Mic Cons Frac L1	0.5	-
Mic Hum Frac L1	0.5	-
Mic Mort Frac L1	0.1	-
RateCoefMic Cons	0.01	1/day
RateCoefMic Mort	0.01	1/day
RateCoefMic Resp	0	1/day
RateCoefSurf Hum	0	1/day
RateCoefSurf L1	0.01	1/day
Gas processes		
AnBal ShapeCoef	100	-
CH4 AerobicOxRate	4.34	/day
CH4 Air Conc	0	g/g
CH4 BubbleRateConstant	180	-
CH4 EbullThreshold	0	-
CH4 HalfRateOxConstant	0	-
CH4 PlantOxidationEff	0.5	-
CH4 RateCoefRatio	1	-
CH4 WaterDiffCoef	0	m2/s
CH4 init Conc	0	g/g
D O2 Tortuosity	0.66	-
H RefTemp	25	C
HenryCoefTempSens	-1700	K
HenryStdCoef cp	0	Mol/atm
IntDiffRedFrac	0.01	-
IntDiffRedFracBase	0	-
Soil water flows		
AScaleSorption	0.5	-
BarrierEfficiency	1	-
BarrierLevel	-1	m
DVapTortuosity	0.66	-
InitialPressuredHead	60	cm water

Table 4.2: CoupModel settings for the methane flux simulation

Setting	Choice	Setting	Choice
Version	Version 3.1, 16 February, 2009	Gas processes	
StartDate	2007-06-24 17:00	Methane Model	Detailed
EndDate	2007-10-22 23:00	Methane emission by plants	on
Stored Output	20	Methane oxidation by plants	on
Number of iterations	96	Oxygen Model	Steady state
		Trace Gas Emissions	Vertical fluxes in soil
Driving Variable	TemperatureAir		
		Model Structure	
Switches		Evaporation	off
Abiotic temp responses	Q10 whole range	GroundWaterFlow	off
		HBV Soil Module	off
		HeatEq	on
Meteorological Data		Irrigation	off
CloudInput	Generated by parameters	LateralInput	No lateral input
DBSunInput	Not Used	Minteq	off
HumRelInput	Generated by parameters	Nitrogen and Carbon	Dynamic interaction with abiotics
PrecInput	Generated by parameters	PlantType	No vegetation
RadGlobInput	Estimated	SaltTracer	off
RadNetInput	Estimated	SnowPack	off
TempAirCycle	Diurnal	SoilVapour	Only SoilVapourflow
TempAirInput	Read from PG-file (first position)	WaterEq	on
TempSurfInput	Not used		
VapourAirInput	As relative humidity	Abiotic driving variables	
WindSpeedInput	Generated by parameters	DeepPercolationInput	Not used
		SoilDrainageInput	Not used
Soil organic processes		SoilInfillInput	Simulated
CN Ratio Influence	no	SoilTempInput	Simulated
Dissolved Organics	off	SoilWaterFlowInput	Simulated
FaecesPool	no	SoilWaterInput	Simulated
Initial Carbon Conditions	As Nitogen and Carbon	WaterStressInput	Simulated
Initial Soil Organic	Linear decrease		
LitterPools	one	Soil Hydraulic	
Microbes	on-substate dependent	Conductivity Function	Mualem
Microbial consumption	F(Temp)	Hydraulic Functions	Brooks and Corey
Microbial mortality	F(Temp)	Matric Conductivity	Function of total conductivity
Organic Uptake	off	Pedo Functions	Not Used
Q Model	off	Replace K-values	No
		Scaling retention	No
Numerical			
FindTimeStep	No	Plant Growth	
NitrogenCarbonStep	TimeResolution determined	Growth	off
NumMethod	Forward Difference	PhotoInput	Simulated
TimeStepOption	Empirical	Root Density Influence	no
Drainage and deep percolation		Soil mineral N processes	
LBoundUnSaturated	No Flow	AmmoniaVolatilisation	off
		Ammonium Mobility	No
Soil water flows		Denit Depth Distribution	Constant
ConvectiveGasFlow	On	Denit Temp Response	Common
Crack	Bypass Flow	Denitrification	Microbial based
Hysteresis	Off	Flexible Uptake	Common for all plants
Initial water conditions	Uniform Pressure Head	Initial Mineral N	Uniform concentration
Soil Water Barrier	On	Nitrific Temp Response	Common
	Nitrification	Old SOILN	
Analytical Solution	Off		
Convection flow	Accounted for	Soil frost	
Heat Pump	Not used	FlowDomains	Low + High Domain
Heat Source	Not used	FrostInteract	InfluencingWater
Initial Heat Conditions	Temp(z)-Estimated	FrostSwelling	On
Lower Boundary	Temperature cycle	Infiltration	Low+High FlowD
PrecTemperature	Equal surface temperature	LoadPotential	On
Vapour flow	Accounted for	k-estimate	MinimiumValues

Lunds Universitets Naturgeografiska institution. Seminarieuppsatser. Uppsatserna finns tillgängliga på Naturgeografiska institutionens bibliotek, Sölvegatan 12, 223 62 LUND.Serien startade 1985. Uppsatserna är även tillgängliga på http://www.geobib.lu.se/

The reports are available at the Geo-Library, Department of Physical Geography, University of Lund, Sölvegatan 12, S-223 62 Lund, Sweden.
Report series started 1985. Also available at http://www.geobib.lu.se/

111. Tränk, L., (2005): Kadmium i skånska vattendrag – en metodstudie i föroreningsmodellering.
112. Nilsson, E., Svensson, A.-K., (2005): Agro-Ecological Assessment of Phonxay District, Luang Phrabang Province, Lao PDR. A Minor Field Study.
113. Svensson, S., (2005): Snowcover dynamics and plant phenology extraction using digital camera images and its relation to CO2 fluxes at Stordalen mire, Northern Sweden.
114. Barth, P. von., (2005): Småvatten då och nu. En förändringsstudie av småvatten och deras kväveretentionsförmåga.
115. Areskoug, M., (2005): Planering av dagsutflykter på Island med nätverkanalys
116. Lund, M., (2005): Winter dynamics of the greenhouse gas exchange in a natural bog.
117. Persson, E., (2005): Effect of leaf optical properties on remote sensing of leaf area index in deciduous forest.
118. Mjöfors, K., (2005): How does elevated atmospheric CO2 concentration affect vegetation productivity?
119. Tollebäck, E.,(2005): Modellering av kväveavskiljningen under fyra år i en anlagd våtmark på Lilla Böslid, Halland
120. Isacsson, C., (2005): Empiriska samband mellan fältdata och satellitdata – för olika bokskogområden i södra Sverige.
121. Bergström, D., Malmros, C., (2005): Finding potential sites for small-scale Hydro Power in Uganda: a step to assist the rural electrification by the use of GIS
122. Magnusson, A., (2005): Kartering av skogsskador hos bok och ek i södra Sverige med hjälp av satellitdata.
123. Levallius, J., (2005): Green roofs on municipal buildings in Lund – Modeling potential environmenta benefits.
124. Florén, K., Olsson, M., (2006): Glacifluviala avlagrings- och erosionsformer I sydöstra Skåne – en sedimentologisk och geomorfologisk undersökning.
125. Liljewalch-Fogelmark, K., (2006): Tågbuller i Skåne – befolkningens exponering.
126. Irminger Street, T., (2006): The effects of landscape configuration on species richness and diversity in semi-natural grasslands on Öland – a preliminary study.
127. Karlberg, H., (2006): Vegetationsinventering med rumsligt högupplösande satellitdata – en studie av QuickBirddata för kartläggning av gräsmark och konnektivitet i landskapet.
128 Malmgren, A., (2006): Stormskador. En fjärranalytisk studie av stormen Gudruns skogsskador och dess orsaker.
129 Olofsson, J., (2006): Effects of human land-use on the global carbon cycle during the last 6000 years.

130 Johansson , T., (2006): Uppskattning av nettoprimärproduktionen (NPP) i stormfällen efter stormen Gudrun med hjälp av satellitdata.
131 Eckeskog, M., (2006): Spatial distribution of hydraulic conductivity in the Rio Sucio drainage basin, Nicaragua.
132 Lagerstedt, J., (2006): The effects of managed ruminants grazing on the global carbon cycle and greenhouse gas forcing.
133 Persson, P., (2007): Investigating the Impact of Ground Reflectance on Satellite Estimates of Forest Leaf Area Index
134 Valoczi, P. (2007): Koldioxidbalans och koldioxidinnehållsimulering av barrskog I Kristianstads län, samt klimatförändringens inverkan på skogen.
135 Johansson, H. (2007): Dalby Söderskog - en studie av trädarternas sammansättning 1921 jämfört med 2005
137 Kalén, V. (2007): Analysing temporal and spatial variations in DOC concentrations in Scanian lakes and streams, using GIS and Remote Sensing
138 Maichel, V. (2007): Kvalitetsbedömning av kväveretentionen i nyanlagda våtmarker i Skåne
139 Agardh, M. (2007): Koldioxidbudget för Högestad – utsläpp/upptag och åtgärdsförslag
140 Peterz, S. (2007): Do landscape properties influence the migration of Ospreys?
141 Hendrikson, K. (2007): Småvatten och groddjur i Täby kommun
142 Carlsson, A. (2008): Antropogen påverkan i Sahel – påverkar människans aktivitet NDVI uppmätt med satellit.
143 Paulsson, R. (2008): Analysing climate effect of agriculture and forestry in southern Sweden at Högestad & Christinehof Estate
144 Ahlstrom, A. (2008): Accessibility, Poverty and Land Cover in Hambantota District, Sri Lanka. Incorporating local knowledge into a GIS based accessibility model.
145 Svensson T. (2008): Increasing ground temperatures at Abisko in Subarctic Sweden 1956-2006
146 af Wåhlberg, O. (2008): Tillämpning av GIS inom planering och naturvård - En metodstudie i Malmö kommun.
147 Eriksson, E. och Mattisson, K. (2008): Metod för vindkraftslokalisering med hjälp av GIS och oskarp logik.
148 Thorstensson, Helen (2008): Effekterna av ett varmare klimat på fenologin hos växter och djur i Europa sedan 1950.
149 Raguz, Veronika (2008): Karst and Waters in it – A Literature Study on Karst in General and on Problems and Possibilities of Water Management in Karst in Particular.
150 Karlsson, Peggy (2008): Klimatförändringarnas inverkan på de svenska vägarna.
151 Lyshede, Bjarne Munk (2008): Rapeseed Biodiesel and Climate Change Mitigation in the EU.
152 Sandell, Johan (2008): Detecting land cover change in Hambantota district, Sri Lanka, using remote sensing & GIS.
153 Elgh Dalgren, Sanna (2008): vattennivåförändringar i Vänern och dess inverkan på samhällsbyggnaden I utsatta städer
154 Karlgård, Julia (2008): Degrading palsa mires i northern Europe: changing vegetation in an altering climate and its potential impact on greenhouse gas fluxes.
155 Dubber, Wilhelm and Hedbom, Mari (2008) Soil erosion in northern Loa PDR

– An evaluation of the RUSLE erosion model

156 Cederlund, Emma (2009): Metodgranskning av Klimatkommunernas lathund för inventering av växthusgasutsläpp från en kommun

157 Öberg, Hanna (2009): GIS-användning i katastrofdrabbade utvecklingsländer

158 Marion Früchtl &Miriam Hurkuck (2009): Reproduction of methane emissions from terrestrial plants under aerobic conditions

159 Florian Sallaba (2009): Potential of a Post-Classification Change Detection Analysis to Identify Land Use and Land Cover Changes. A Case Study in Northern Greece

160 Sara Odelius (2009): Analys av stadsluftens kvalitet med hjälp av geografiska informationssystem.

161 Carl Bergman (2009): En undersökning av samband mellan förändringar i fenologi och temperatur 1982-2005 med hjälp av GIMMS datasetet och klimatdata från SMHI.

162 Per Ola Olsson (2009): Digitala höjdmodeller och höjdsystem. Insamling av höjddata med fokus på flygburen laserskanning.

163 Johanna Engström (2009): Landskapets påverkan på vinden -sett ur ett vindkraftperspektiv.

164 Andrea Johansson (2009): Olika våtmarkstypers påverkan på CH_4, N_2O och CO_2 utsläpp, och upptag av N_2.

165 Linn Elmlund (2009): The Threat of Climate Change to Coral Reefs

166 Hanna Forssman (2009): Avsmältningen av isen på Arktis - mätmetoder, orsaker och effekter.

167 Julia Olsson (2009): Alpina trädgränsens förändring i Jämtlands- och Dalarnas län över 100 år.

168 Helen Thorstensson (2009): Relating soil properties to biomass consumption and land management in semiarid Sudan – A Minor Field Study in North Kordofan

169 Nina Cerić och Sanna Elgh Dalgren (2009): Kustöversvämningar och GIS - en studie om Skånska kustnära kommuners arbete samt interpolations-metodens betydelse av höjddata vid översvämningssimulering.

170 Mats Carlsson (2009): Aerosolers påverkan på klimatet.

171 Elise Palm (2009): Övervakning av gåsbete av vass – en metodutveckling

172 Sophie Rychlik (2009): Relating interannual variability of atmospheric CH_4 growth rate to large-scale CH_4 emissions from northern wetlands

173 Per-Olof Seiron and Hanna Friman (2009): The Effects of Climate Induced Sea Level Rise on the Coastal Areas in the Hambantota District, Sri Lanka - A geographical study of Hambantota and an identification of vulnerable ecosystems and land use along the coast.

174 Norbert Pirk (2009): Methane Emission Peaks from Permafrost Environments: Using Ultra–Wideband Spectroscopy, Sub-Surface Pressure Sensing and Finite Element Solving as Means of their Exploration

175 Hongxiao Jin (2010): Drivers of Global Wildfires — Statistical analyses

176 Emma Cederlund (2010): Dalby Söderskog – Den historiska utvecklingen

177 Lina Glad (2010): En förändringsstudie av Ivösjöns strandlinje